CONF-9605186--

Proceedings of the

FOURTEENTH SYMPOSIUM ON ENERGY ENGINEERING SCIENCES

Mechanical Sciences; Solids and Fluids

May 15-16, 1996
at
Argonne
National Laboratory
Argonne, Illinois

CONF-9605186--

Proceedings of the

FOURTEENTH SYMPOSIUM ON ENERGY ENGINEERING SCIENCES
Mechanical Sciences; Solids and Fluids

May 15-16, 1996

at

ARGONNE NATIONAL LABORATORY

Argonne, Illinois

Cosponsored by

Office of Basic Energy Sciences
U.S. DEPARTMENT OF ENERGY

and

Energy Technology Division
ARGONNE NATIONAL LABORATORY

Coordinated by

Argonne National Laboratory
9700 South Cass Avenue
Argonne, Illinois 60439

Conference Number: 9605186

Do Not Do Analytics on these

Conference 9605186

14. symposium on energy engineering sciences: mechanical sciences; solids and fluids, Argonne, Illinois, 15-17 May 1996

Entered: 06/18/96
Changed: 10/04/96

Papers : 2
Volumes: 1

Activities: 0
Sponsors : 2

Energy Meetings:

Conference Paper 1 of 2

Author : Mondy, L. A.
Report Number: SAND--96-1384C
Secondary : CONF-9605186--1
Trac No. SC: : M96011839

Entered : 06/18/96
Changed :
Description:
Note :

Microstructure and momentum transport in concentrated suspensions

Conference Paper 2 of 2

Author : Telschow, K. L.
Report Number: INEL--96/00162
Secondary : CONF-9605186--2
Trac No. SC: : M96014122

Entered : 09/05/96
Changed :
Description:
Note :

Calculation and measurement of the critical state in superconducting tapes

FOURTEENTH SYMPOSIUM ON ENERGY ENGINEERING SCIENCES
Mechanical Sciences; Solids and Fluids

FOREWORD

This Proceedings Volume includes the technical papers that were presented during the Fourteenth Symposium on Energy Engineering Sciences on May 15-16, 1996, at Argonne National Laboratory, Argonne, Illinois. The Symposium was organized into seven technical sessions, which included 26 individual presentations followed by discussion and interaction with the audience. A list of participants is appended to this volume.

This was the fourteenth annual Symposium sponsored by the Engineering Research Program of the Office of Basic Energy Sciences of the U.S. Department of Energy. The technical areas encompassed in this year's Symposium were mostly from solid and fluid dynamics. Each paper dealt with the research effort being sponsored by the Engineering Research Program.

The DOE Office of Basic Energy Sciences, of which Engineering Research is a component program, is responsible for the long-term mission-oriented research in the Department. It has the prime responsibility for establishing the basic scientific foundation upon which the Nation's future energy options will have to be identified, developed, and built. It is committed to the generation of new knowledge necessary for the solution of present and future problems of energy exploration, production, conversion, and utilization, consistent with respect for the environment.

Consistent with the DOE/BES mission, the Engineering Research Program is charged with the identification, initiation, and management of fundamental research on broad, generic topics addressing energy-related engineering problems. Its stated goals are: 1) to improve and extend the body of knowledge underlying current engineering practice so as to create new options for enhancing energy savings and production, for prolonging useful life of energy-related structures and equipment, and for developing advanced manufacturing technologies and materials processing with emphasis on reducing costs with improved industrial production and performance quality; and 2) to expand the store of fundamental concepts for solving anticipated and unforeseen engineering problems in the energy technologies.

In achieving these goals, the Engineering Research Program supports approximately 130 research projects covering a broad spectrum of topics cutting across traditional engineering disciplines with a focus on three areas: 1) mechanical sciences, 2) control systems and instrumentation, and 3) engineering data and analysis. The Fourteenth Symposium involved approximately one-fifth of the research projects currently sponsored by the DOE/BES Engineering Research Program.

The Fourteenth Symposium was held under the joint sponsorship of the DOE Office of Basic Energy Sciences and Argonne National Laboratory. Local arrangements were handled by Ms. Jacquie Habenicht of ANL Conference Services. Ms. Nina Daly of the ANL Office of Technical Communication Services was responsible for assembling these proceedings and attending to their publication.

I am grateful to all who contributed to the success of the program, particularly to the participants for their excellent presentations and their active involvement in discussions. The resulting interactions made this Symposium a most stimulating and enjoyable experience.

Robert Goulard, ER-15
Division of Engineering and Geosciences
Office of Basic Energy Sciences

FOURTEENTH SYMPOSIUM ON ENERGY ENGINEERING SCIENCES

May 15-16, 1996

Argonne National Laboratory

Argonne, IL

TABLE OF CONTENTS

Technical Session 3 - Materials II

Technical Session 4 - Controls

Technical Session 5 - Fluid Mechanics I

PHOTOTHERMAL MEASUREMENTS OF SUPERCONDUCTORS

G. S. Kino, W. R. Studenmund and I. M. Fishman

Ginzton Laboratory, Stanford University
Stanford, California 94305-4085

ABSTRACT

A photothermal technique has been used to measure diffusion and critical temperature in high temperature superconductors. The technique is particularly suitable for determining material quality and inhomogeneity.

INTRODUCTION

We have been developing a new photothermal microscope technique for studying high-temperature superconductors. The microscope measures differential optical reflectivity (DOR) and thermal diffusivity in thin films and single crystals of cuprate superconductors. Both normal and superconducting phases are characterized. The spatial resolution of the DOR technique is comparable to an optical microscope and allows us to measure small samples several microns in extent. The photothermal technique is extremely sensitive to manifestations of optical and thermal parameters affected by phase transitions, and in particular, to the superconductive transition in high-T_c materials.

Modern technology is able to produce very-high-quality, high-temperature superconducting samples. However, the best available high-T_c samples have a single domain size (~100 μm). Traditional methods of sample characterization (DC and microwave techniques) used for measurements of critical temperature, critical current, and material uniformity have a spatial resolution of ~1 mm.[1,2,3] With our technique, one can measure optical reflectivity and critical temperature with the spatial resolution of an optical microscope (1-2 μm). We can determine the variation of the critical temperature from point to point, and measure the quality of the material, by determining its diffusivity and differential optical reflectivity as a function of temperature. We can also determine the anisotropy of the material in small regions, and hence determine whether it is a single crystal or twinned. Thus, we believe that we have arrived at an excellent method for testing the quality of high-temperature superconducting materials.

For the first time, we used a polarized light probe to observe the anisotropy of single crystals. With it we observe an extremely sharp peak in the probe DOR signal near the critical temperature when the light is polarized along the a axis, and a very different characteristic output as a function of temperature when the light is polarized along the b axis.

THE EXPERIMENT

The basic microscope configuration is shown in Fig. 1. A He-Ne laser (632 nm), acousto-optically modulated by a Bragg cell, is focused on the sample and used as a heating beam; this beam periodically modulates the temperature of the sample at the focus and excites a thermal wave with a diffusion length of the order of 50 μm. Within a few microns from the focus of the heating beam, an infrared semiconductor laser (780 nm) is focused on the sample to probe the reflectivity change due to the temperature variation caused by the thermal wave. We have chosen a semiconductor laser for its minimum noise

and select, with a dichroic (lowpass) filter, the reflected probe laser light which impinges on a PIN photodiode. The phase and amplitude of the modulated signal are measured with a lock-in amplifier.[4]

The photothermal microscope designed for measuring high-temperature superconductors consists of three main components: (1) the optical system of the microscope, which excites and detects the thermal wave, (2) the temperature-controlled cryostat, which houses the sample and carries out the temperature sweep necessary for the measurement, (3) an auto-focusing feedback system, which ensures that the sample always stays at the focal plane of the microscope objective during a temperature sweep, and (4) computer control.[4]

We have combined a photothermal microscope with a high-vacuum cryostat to measure the thermal diffusivity of high-T_C superconductors as a function of temperature. The micron resolution obtained by using such a system allows us to measure single-crystal samples which are too small or irregular to be measured by standard bulk techniques. Therefore, we have the ability to measure the full anisotropic conductivity and measure diffusion within a single crystal or across a grain boundary.

For highest-resolution imaging, we make the two laser beams coincident and measure the amplitude of the reflectivity change. In this manner we can obtain resolutions limited only by the spot size of the microscope objective used for the focusing. For quantitative measurements of the thermal diffusivity in a specific direction, we separate the heating and probe beams by a known distance and measure the thermal phase lag between the two. For distances greater than a few spot widths, the phase lag between two points a distance x apart is $\phi_x = x\sqrt{2\omega / D_x}$, where ω is the heating frequency and D_x is the thermal diffusivity in the x direction.[5] Measurement of thermal phase has the great advantage that it is insensitive to nonthermal effects, such as laser intensities and the variation of refractive index with temperature.

The vacuum inside the cryostat is controlled to be under 2×10^{-7} torr to limit ice on the sample surface to less than 1 μm during the two hours needed for the measurement. A vac ion pump is used with a

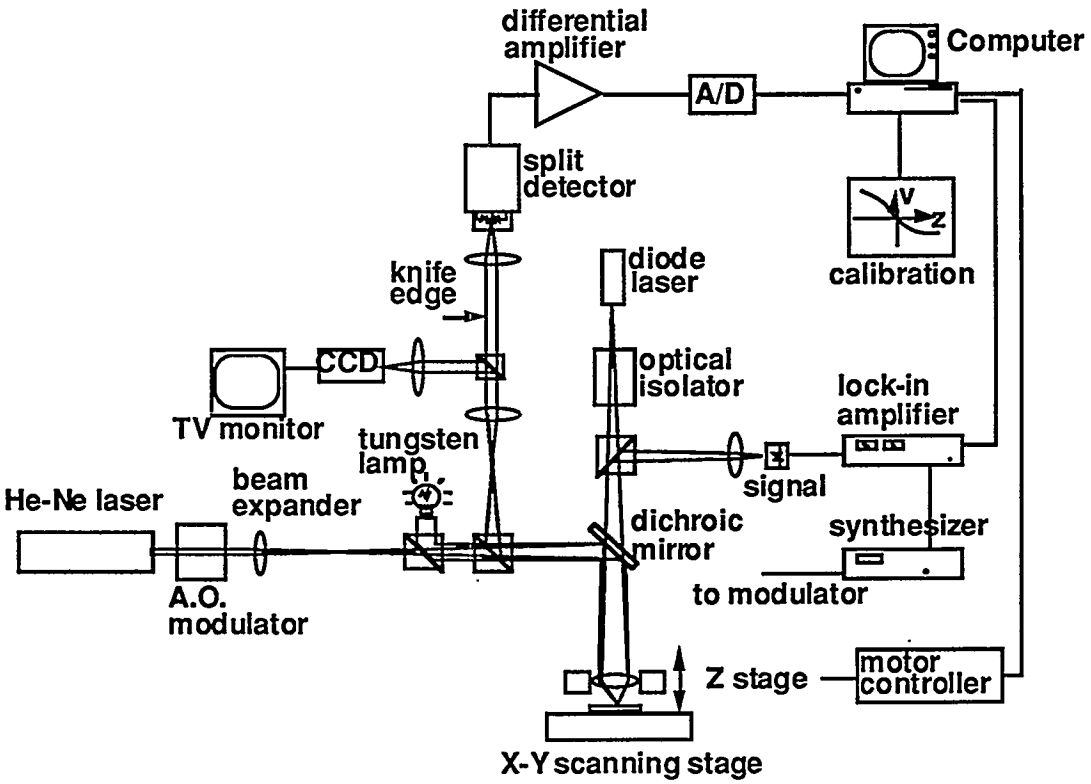

Fig. 1. System for photothermal measurements of superconductors.

gettering pump because of its small size, low weight, low ultimate vacuum, and oil-free operation. This ensures a system free of vibration, and makes it possible to mount the cryostat on a micropositioning system. The focused light beams are incident on the sample passing through a long working distance (7 mm) 0.3 NA objective and a 100 μm thick silica window mounted on the vacuum housing which is made thin to reduce aberration of the focused light.

Special precautions have been taken to ensure an accurate temperature reading of the sample. We limit the power of both heating and probe lasers to only a few tens of microwatts. A three-dimensional theoretical simulation indicates that the dc rise in the surface temperature of the sample caused by laser heating by the pump is less than 2 K, and that by the probe is less than 0.5 K. The temperature reading of a silicon sensor attached to the sample mount is verified with an in-situ ac susceptibility measurement. Underneath the sample, two coils are embedded in a sapphire sample mount, which provides electrical insulation from, but a good thermal conducting path to, the copper block of the cryostat. The larger coil is driven with an ac current; the voltage induced in the smaller coil is measured with a lock-in amplifier. A sharp change in the induced voltage indicates the superconducting transition and calibrates the reading of the silicon sensor.

During the cooling or heating of the cold finger, the tip of the stage tends to move as a result of mechanical contraction or expansion. Large vertical movement of the sample can result in a loss of focus and cause an error in the photothermal signal. We therefore incorporate an autofocusing mechanism to adjust the z-position of the objective and to ensure that the sample surface is always in the focal plane of the objective. A focusing accuracy of 1 μm is easily achieved in our measurements; the error is well within the depth of focus (5 μm) of the 0.33 numerical aperture objective.

The lateral movement of the sample, too, can cause noise in the signal output because of the nonuniformity of the sample reflectance. Therefore, the x- and y-directional movement of the sample is monitored with the CCD camera and is compensated for manually with a motorized stage. The accurate lateral definition (±3 μm) of the experiment allows us to achieve measurements of the thermal diffusivity within one domain of single-crystal high-T_C superconductors.

Phase Measurements of Diffusion: Measurements of the diffusion as a function of temperature in YBCO are shown in Fig. 2. A major advantage of measuring within a small volume is demonstrated by these results, where the diffusivity measurements were conducted for a 10 μm spacing between the excitation and the probe areas in a single YBCO domain, and across the twin boundary. For comparison, the diffusivity measurements for thin YBCO films using another optical technique, the transient grating method, in a region 200 μm across, are also shown. It will be seen that, above the transition temperature, the thermal diffusivity decreases slowly with temperature. The diffusivity measured over large-area thin film samples (200 μm across), and across a grain boundary, agree with bulk measurements, but the diffusivity measured within a grain is approximately twice as large as the measured value across a grain boundary. This is an interesting result, for it indicates that there must be a large change in temperature across the grain boundary, and tends to indicate that phonons (presumably optical phonons) and normal electrons (which contribute to diffusion) are reflected at the grain boundary.[6]

Below T_C, the data for different samples differs dramatically. For the single domain for $T < T_C$, diffusivity increases sharply over two orders of magnitude. This diffusivity enhancement can be explained only by removal of free carriers from the conducting state into the superconducting condensate. For samples of lower quality, the enhancement is not that sharp, especially for the thin film sample where the superconducting transition has almost no effect upon the diffusivity. The measurement through the twin boundary is intermediate between the other two curves. The twin boundary, though thin compared to the beam spacing, creates significant additional resistance for heat transfer. The diffusivity enhancement is evidence of the phonon mechanism of heat transfer inside a single domain. This conclusion does not differ from the traditional viewpoint on heat transfer in high-T_C materials. In thin films, additional mechanisms of phonon scattering, such as scattering by point defects independent of the free carrier density, probably dominate. The experimental results obtained show very conclusively that the scattering rate of phonons is proportional to the number density of normal electrons at temperatures below T_C.[1,6,7,8]

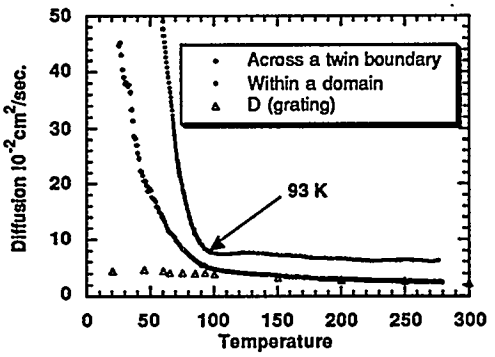

Fig. 2. Measured diffusion in YBCO.

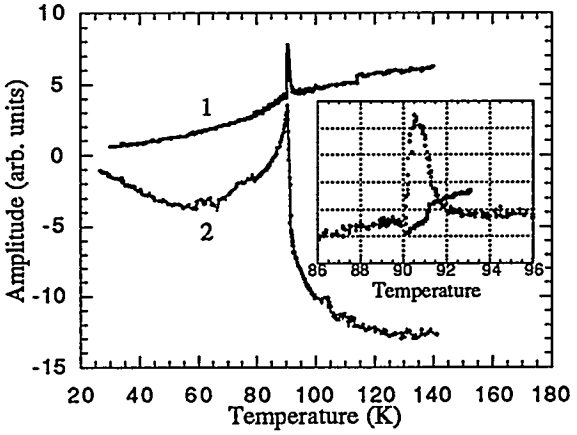

Fig. 3. Temperature dependence of differential reflectivity for the probe beam polarization along the *a* axis (1), and along the *b* axis (2), of a single YBCO domain. Inset: curve 1 in the vicinity of T_C together with the inductive coil response indicating the transition temperature.

Furthermore, the number density of normal electrons varies with temperature much like the predictions of BCS theory, although there is a considerable difference between the experiment and theory near T_C (see Fig. 4).

Differential Optical Reflectivity (DOR) Measurements: In the visible range, the optical constants of high-T_C superconducting materials do not show any noticeable temperature dependence.[9] However, in the vicinity of the critical temperature T_C, the perturbation caused by the transition, though small, is rather sharp and may be detected by a differential technique. Here, we will describe photothermal measurements of differential optical reflectivity (DOR) of single $YBa_2Cu_3O_{7-x}$ crystals[4] and the temperature variation of the thermal wave amplitude response. It is worth mentioning that, though the amplitude and the phase of the thermal wave carry different information, they are obtained in the same experiment.

One set of YBCO samples used in this study was twinned, with critical temperatures in the range of 60-93 K. The modulated signal did not show any anisotropy and polarization dependence. Another set of

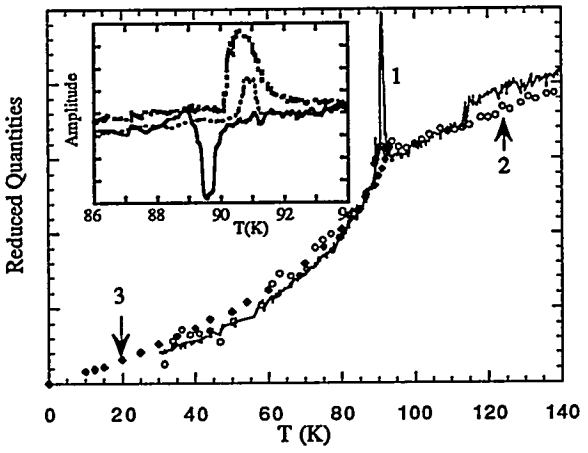

Fig. 4. Comparison of temperature-dependent DOR response in the "a" polarization (curve 1, same as curve 1 in Fig. 1), data for thermal resistance (curve 2, open circles) calculated from thermal wave phase,[6] and for the normal component density (curve 3, solid squares) calculated from microwave measurements.[14] Inset: DOR peaks in the vicinity of T_C for the first sample (top curve, same as curve 1 in this figure), and for two domains of the second sample.

measurements were made with far higher quality single crystals with domain sizes in the 200-500 μm range. In this case we used polarized light for the probe and were able to rotate the angle of polarization of the incident light. Two samples investigated in this study were single YBCO crystals with a critical temperature of 91.2 K. Both samples had comparatively large untwinned areas of approximately 50×200 μm. These areas were imaged under a polarizing microscope as dark and light domains. All measurements were conducted in the *a-b* plane. Standard reflectivity measurements with polarized light on both samples show distinct anisotropy of the reflectivity R in the *a-b* plane, described by:

$$R = A + B\cos 2\theta \qquad (1)$$

with a B/A ratio of 2.56, which is in good agreement with the results obtained on similar samples by Cooper et al[9] [for an optical energy of ~1.5 eV]. This behavior is expected for the reflection from an *a-b* plane with enhanced polarizability along the Cu-O chains oriented along the *b* direction.

Like the results obtained previously on heavily-twinned YBCO samples, the single-domain DOR data for a given probe polarization in Fig. 3 consists of a continuous smooth "background" in the entire temperature range 20-300 K, and a sharp peak in the vicinity of T_C. In earlier measurements we were able to show that the smooth background appears to be associated with the normal component.[6] For a peak-to-peak temperature modulation of approximately 0.2 K, the maximum observed signals are about 10^{-4} of the average reflected intensity of the probe beam. Integration of the DOR response with respect to temperature shows that R changes by less than 1% in the temperature range 20-120 K.

Over most of the temperature range, as might be expected for an anisotropic material with zero off-diagonal terms in the dielectric or reflectivity matrices associated with optical rotation, the DOR data shows angular anisotropy of the same form as in standard reflectivity measurements,[9] but the coefficients A and B vary rapidly with temperature near the critical temperature. Above the critical temperature the DOR response is a weak function of temperature. As we have already discussed, the angular dependence of the DOR signal is of the same form as in the standard reflectivity measurements. However, unlike the results obtained with our earlier measurements of highly-twinned samples, when the polarization vector rotates from *a* to *b*, the DOR signal changes sign,[10] as may be seen in curves 1 and 2 of Fig. 3.

To describe this sign change and some other features of the DOR signal, we use a two-component Drude model[11,12] with a dielectric constant ε of the form:

$$\varepsilon = 1 - \frac{(1-f)\omega_p^2}{\omega^2 + i\Gamma_1\omega} - \frac{f\omega_p^2}{\omega^2 + i\Gamma_2\omega} \tag{2}$$

where ω_p, Γ_1 and Γ_2 are the plasma frequency and electron collision rates for the normal and superconducting phases, respectively, and f is the fraction of superconducting electrons ($f = 0$ for $T > T_c$). The reflection coefficient is

$$R = \left|(\sqrt{\varepsilon} - 1)/(\sqrt{\varepsilon} + 1)\right|^2$$

For small $\Gamma \ll \omega$, $\Gamma \ll \omega_p$, the DOR response takes the form:

$$\frac{dR}{dT} = \frac{2R_0\Gamma_1}{\omega^2 - \omega_p^2}\left[(1-f)\frac{d(\delta\Gamma)}{dT} - \frac{df}{dT}\delta\Gamma\right] \tag{3}$$

where $\delta\Gamma = (\Gamma_1 - \Gamma_2) \ll \Gamma_1$ or Γ_2, $|\omega - \omega_p| \gg \Gamma_1$ or Γ_2, R_0 is the reflection coefficient for an unmodulated probe beam, and it is assumed that $|d\Gamma_2/dT| \ll |d(\delta\Gamma)/dT|$. The DOR signal sign depends on the relation between the incident frequency ω and the plasma frequency ω_p. From comparison with the standard reflectivity measurements in single domains, we expect that the probe frequency ($\lambda = 0.78$ μm) is positioned between the plasma frequencies for the a and b directions.

Beyond the sign reversal, Eq. (3) also predicts that the DOR signal consists of two components proportional to the rates of change of $\delta\Gamma$ and the fraction of superconducting phase f with temperature, respectively. In agreement with this prediction, the DOR response consists of a continuous smooth "background" in the entire temperature range 20-300 K, and a sharp peak in the vicinity of T_c. The background is associated with the normal component response. Above T_c ($f = 0$); only this component is present in the DOR signal. Below T_c the background amplitude decreases and at $T \sim 20K$ practically disappears. Equation (3) predicts that below T_c the first term should decrease with temperature as (1 - f), or the density of the normal component. This prediction allows for comparison with other experiments where the density of the normal component was measured.

In Fig. 4, the densities of the normal component derived from microwave penetration depth (curve 2)[12] and thermal diffusivity (curve 3)[6] measurements are compared with the DOR signal for the "a" polarization (curve 1). The comparison shows similarity of the temperature dependencies for all three measurements, which confirms that the Drude model may be applied, at least for qualitative analysis of what appears to be the normal component of the DOR data. Some noticeable differences may be explained by the temperature dependence of $d(\delta\Gamma)/dT$ below T_c.

We can therefore associate the "smooth" parts of the curves with normal electrons, but the peaks with the superconductive carriers. At the present time, it is difficult to give a good explanation of the behavior near the peaks. Fluctuation theory seems to be inadequate for the purpose, as is BCS theory, and we do not yet have a good explanation of why the peak can change in sign, as shown in the inset of Fig. 4.

Measurement of the Periodic Temperature Variation: Differential optical reflectivity data taken on single-domain samples shows very sharp functions of temperature. Since the resolution of the method is dependent on the variation of temperature caused by the pump heating, there has been some question as to whether our assumption of a small temperature variation is adequate. Our theoretical estimates predicted a 0.2 K variation at the probe. However, there was no direct experimental evidence that our evaluations are correct. We, therefore, developed a method for determining AC temperature variation, based on comparison of the amplitudes of the fundamental (ω) and second harmonic (2ω) components in the reflected signal. The reflection coefficient R may be written as a Taylor expansion in terms of the temperature variation ΔT:

$$R = R_0 + \frac{dR}{dT}\Delta T + \frac{d^2R}{dT^2}\frac{(\Delta T)^2}{2} + \ldots \tag{4}$$

where the periodic variation of temperature ΔT is $\Delta T = \theta \cos \omega t$. It then follows from Eq. (4) that

$$R \approx R_0 + \frac{dR}{dT}\theta \cos \omega t + \frac{d^2R}{dT^2}\frac{\theta^2}{4}\cos 2\omega t \tag{5}$$

The last relation provides a convenient method of measuring the amplitude of the periodic temperature variation. The ω component is proportional to $\theta\, dR/dT$; the 2ω component is proportional to $(\theta^2/4)d^2R/dT^2$. Integrating the 2ω component, we can obtain the value of $(\theta^2/4)dR/dT$. Comparison with the coefficient of the ω component provides a direct measurement of θ. In Fig. 5 the results of these measurements are shown; curve (a) is the first harmonic signal and curve (b) shows the integral of the 2nd harmonic signal over temperature. We measured the small amount of 2nd harmonic in the input signal due to the chopper not being entirely symmetric, and arrived at a value of 0.01 of the 1st harmonic. By taking account of this leakage and the larg2er rate of attenuation of the 2nd harmonic signal, we corrected curve (b) by subtraction of 0.005 of the 1st harmonic signal from it before integration. This process yielded curve (c). It will be seen that two curves representing the differential reflectivity at ω and the integral of the data at 2ω have similar temperature dependences, which agrees with the results of Eqs. (2) and (3).

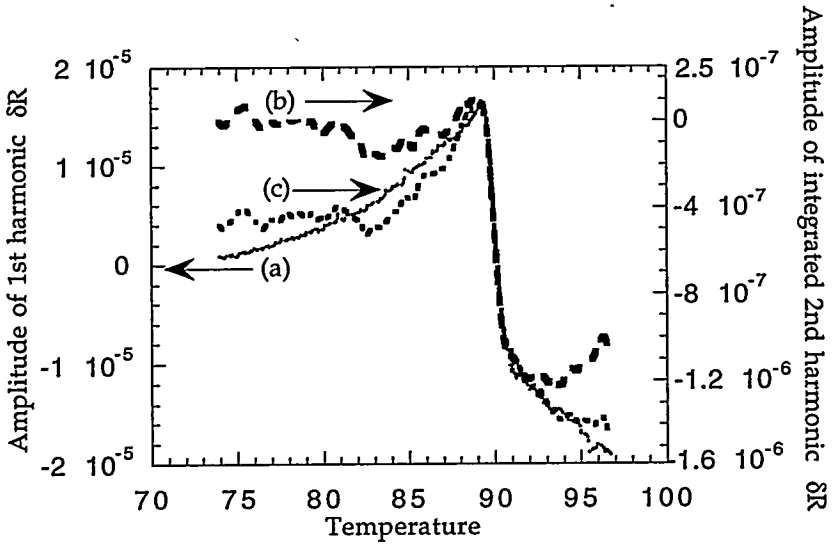

Fig. 5. Comparison of (a) 1st harmonic, (b) integrated 2nd harmonic signal, and (c) integrated 2nd harmonic signal with 0.005 leakage of 1 - f signal with polarization along the *b* axis.

CONCLUSION

The photothermal technique provides information on inhomogeneity, the value of the critical temperature in small regions, and measurements of diffusion (and hence the normal carrier density below the critical temperature). New information has been obtained on the behavior of highly anisotropic single crystals near the critical temperature, and on the temperature variation caused by the measurement process itself. The apparatus is being redesigned to make it more stable and easy to use so that materials researchers can make routine use of it.

ACKNOWLEDGMENT

This work was performed under the auspices of the U.S. Department of Energy. The authors would like to thank J. Giapintzakis of D. Ginsberg's laboratory for the supply of high-quality samples of YBCO, and W. Hardy, and S. Doniach for many useful discussions.

REFERENCES

1. C. Uher, J. Supercond., 3, 337 (1990).

2. R. C. YU, M. B. SALAMON, JIAN PING LU, AND W. C. LEE, Phys. Rev. Lett. 69, 1431 (1992).

3. J. L. COHN, E. F. SKELTON, S. A. WOLF, J. Z. LIU, AND R. N. SHELTON, Phys. Rev. B45, 13144 (1992).

4. X. D. WU, J. T. FANTON, G. S. KINO, AND A. KAPITULNIK, "A Photothermal Microscope for High-T_c Superconductors and Charge Density Waves," Rev. of Scientific Instruments 64, 3321-3327 (1993).

5. J. G. FANTON, D. B. MITZI, A. KAPITULNIK, B. T. KHURI-YAKUB, G. S. KINO, D. GAZIT, AND R. S. FEIGELSON, "Photothermal Measurements of High-T_c Superconductors," Appl. Phys. Lett. **55** (6), 598-599 (7 August 1989)

6. I. M. FISHMAN, G. S. KINO, AND X. D. WU, "Density of Normal Carriers Below T_C and Thermal Resistance of Twin Boundaries in $YBa_2Cu_3O_{7-x}$ Single Crystals," Phys. Rev. B (Condensed Matter) **50**, 7192-4 (1994).

7. L. TEWORDT AND TH. WOLKHAUSEN, Solid State Comm. 70, 839 (1989).

8. L. TEWORDT AND TH. WOLKHAUSEN, Solid State Comm. 75, 515 (1990).

9. S . L. COOPER, D. REZNIK, A. KOTZ, M. A. KARLOW, R. LIU, M. V. KLEIN, W. C. LEE, J. GIAPINTZAKIS, D. M. GINSBERG, B. W. VEAL AND A. P. PAULIKAS, Phys. Rev. B 47, 8233 (1993).

10. I. M. FISHMAN, G. S. KINO, X. D. WU, AND W. R. STUDENMUND, A. A. ABRIKOSOV, A. A. VARLAMOV, AND A. I. BUZDIN, Physica C 249, 304 (1995).

11. T. TIMUSK AND D. B. TANNER, in *Physical Properties of High Temperature Superconductors* I, Ed: D. M. Ginsberg, p.339 (World Scientific, Singapore, 1989).

12. W. N. HARDY, D. A. BONN, D. C. MORGAN, RUIXING LIANG, AND KUAN ZHANG, Phys. Rev. Lett. 70, 3999 (1993).

SCANNED PROBE MICROSCOPY FOR THIN FILM SUPERCONDUCTOR DEVELOPMENT *

John Moreland

Electromagnetic Technology Division
National Institute of Standards and Technology
Boulder, Colorado 80303, USA

ABSTRACT

Scanned probe microscopy is a general term encompassing the science of imaging based on piezoelectric driven probes for measuring local changes in nanoscale properties of materials and devices. Techniques like scanning tunneling microscopy, atomic force microscopy, and scanning potentiometry are becoming common tools in the production and development labs in the semiconductor industry. We present several examples of applications specific to the development of high temperature superconducting thin films and thin-film devices.

INTRODUCTION

Rapid advances in high temperature superconductor (HTS) technology have lead researchers to consider replacing normal metals in several electronic applications including transmission lines, filters, and on-chip as well as multi-chip module interconnects. HTS filters and interconnects have the advantages of low-losses and frequency independent dispersion. In particular, Ajimine, *et al.*[1] have demonstrated the usefulness of a yttria stabilized zirconia (YSZ) layer as a gate insulator between $YBa_2Cu_3O_x$ (YBCO) films and Si substrates. Harvey, *et al.*[2] have made low resistivity contact structures between YSZ/YBCO/Ag trilayers and Si using ion-milled, Au-filled vias with contact resistance's of 10^{-6} Ω-cm^2. Ekin, *et al.*[3] have made significant progress towards optimizing YBCO contact processes that would be compatible with Si integrated circuit processing.

It is clear that HTS thin-film properties are affected by nanometer-scale morphology and electronic processes which directly or indirectly influence the performance of various HTS interconnect devices. Measurements of roughness, critical dimensions, field patterns, and local electronic processes provide information about the

fundamental operation and ultimate performance limitations and are thus critical in the development process. Scanned probe microscopies[4] (SPM) such as scanning tunneling microscopy (STM),[4] atomic force microscopy (AFM),[5] and scanning potentiometry[6] are examples of imaging techniques that are uniquely qualified for these applications because of the nanometer-scale dimensions of the various scanning probes. The purpose of this paper is to demonstrate the usefulness of SPM technology in the development of HTS interconnect devices by presenting several example applications.

MORPHOLOGY AND SURFACE DENSITY OF STATES OF YBCO FILMS

The growth habit of the YBCO films depends on the deposition technique and substrate material.[7,8,9] For example, Fig. 1a shows screw dislocation growth on the surface of a sputtered film on MgO as imaged by STM. Substrate dislocations seed YBCO spiral growth with an average spacing of 1 μm. Many spirals appear to merge into each other within the surface of a single grain of several micrometers in diameter.

The STM growth step height for all of the films measured at room temperature are anomalously large compared to the theoretical unit cell in the c-axis direction. We believe that variations in the surface barrier, density of states, or similar electronic effects cause these anomalies and that they do not represent the true topography of the samples. Hawley, *et al.* have seen similar anomalies in STM data.[10] They have shown, however, by performing AFM, which is relatively unaffected by the surface density of sates, that the true step height is about 1 nm as expected.

The STM step height is temperature dependent. As the temperature decreases from 300 K the growth step height decreases, approaching the expected unit cell value of 1.2 nm at 76. The origin of this striking temperature effect is uncertain. Perhaps there is a semiconducting layer consisting of de-oxygenated YBCO on the films that undergoes carrier freeze-out upon cooling. Carrier freeze out would have the effect of changing the density of states at the surface of the film. In the extreme case of complete freeze-out, the shape of the tunneling barrier between the film and the STM tip may be affected as the layer becomes insulating. Alternatively, at lower temperatures as the Cu-O planes decouple and conduction becomes more 2D in character, the rate for tunneling perpendicular to the Cu-O planes may be affected. Generally, measurements of the resistivity anisotropy for single crystals of YBCO support this possibility. Regardless of the cause, surface density of states of effects will dominate the interface transport properties of YBCO films which are critical to many prospective interconnect technologies.

Comparison of STM and AFM images of YBCO thin-film samples has lead to another interesting observation regarding HTS film growth. AFM images reveal a high density of small distinct nanoparticles, 10 to 50 nm across and 5-20 nm high, which do not appear in the STM images of the same samples as shown in Fig 1b.[11] During STM scanning of the sample, the STM tip breaks off the particles and moves them to the edge of the scanned area. The presence of the particles, which are thought to be yttria,[12] seems to be generic for many types of YBCO thin-films regardless of film thickness or substrate. One intriguing possibility is that the insulating nanoparticles, affectionately referred to as "sand" (as opposed to the much larger "boulders" often observed on laser ablated YBCO thin films), might be the natural pinning sights responsible for the high critical currents of these films. Thus far the microscopic (or nanoscopic, as the case may be) nature of the pining sites has eluded scientists. In any case, the knowledge of the presence of the sand is important for the development of YBCO thin films in multilayer structures for electronic applications of HTS films.

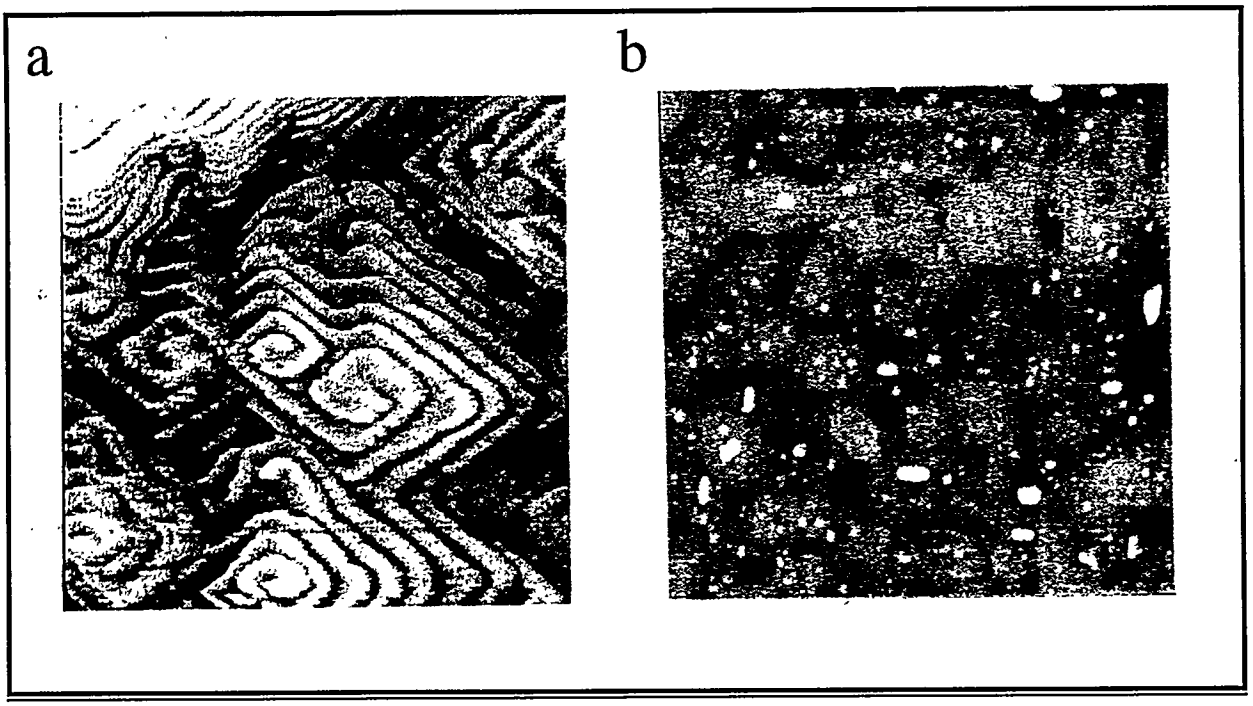

Fig. 1. a) 1 μm STM image of surface density of states "topography" of a YBCO film deposited on a MgO substrate (from ref.9). b) 2.5 μm AFM image of yttria sand on a YBCO film deposited on a $LaAlO_3$ substrate (from ref.11).

YBCO FILM GROWTH ON Si SUBSTRATES

We have studied YBCO thin films deposited on Si substrates.[13] The deposition method was developed by Fork *et al.*[14] and relies on a thin film of YSZ as a chemical buffer as well as a strain layer to reduce lattice-mismatch strain between the YBCO and the Si. R-T measurements of unpatterned films show T_c ranging from 85 to 87 K with a resistivity ratio R_{300K}/R_{100K} of about 2.5. Typically, J_c is 9 x 10^5 A/cm^2 at 4 K. X-ray diffraction shows that the YSZ and the YBCO are c-axis oriented with the YSZ layer having good epitaxy on the Si and the YBCO layer having both a-axis and b-axis oriented grains within the plane of the film.

One of the purposes of a YSZ layer is to prevent chemical reaction between the Si substrate and the YBCO film. Ideally, the YSZ layer should be continuous. However, even if there are pinholes in the YSZ, it is generally thought that they are small in diameter, few in number, and that the reaction product between the YBCO and Si is itself an insulator. This means that the pinholes cannot be detected electrically by measuring conduction leakage between the Si and YBCO. Figure 2a is an AFM image of a YSZ film that was removed from the vacuum system before depositing YBCO. Pinholes penetrating the film are readily visible. The pinhole density is 50/μm^2. The pinholes vary in size with the majority being about 15 nm in diameter. The largest pinhole observed was 44 nm and the smallest was 5 nm. This is direct proof of the existence of pinholes in YSZ buffer layers. Other significant aspects of Fig. 2a are that there is no evidence of cracking in the YSZ film and that, aside from the pinholes, the film is very flat with less than 1 nm roughness indicating good epitaxy on the Si.

Pinholes may be one of several factorsalong with YBCO film strain and cracking that may cause a reduction in T_c and J_c from the highest values observed for films deposited on $LaAlO_3$ of T_c = 91.5 K and

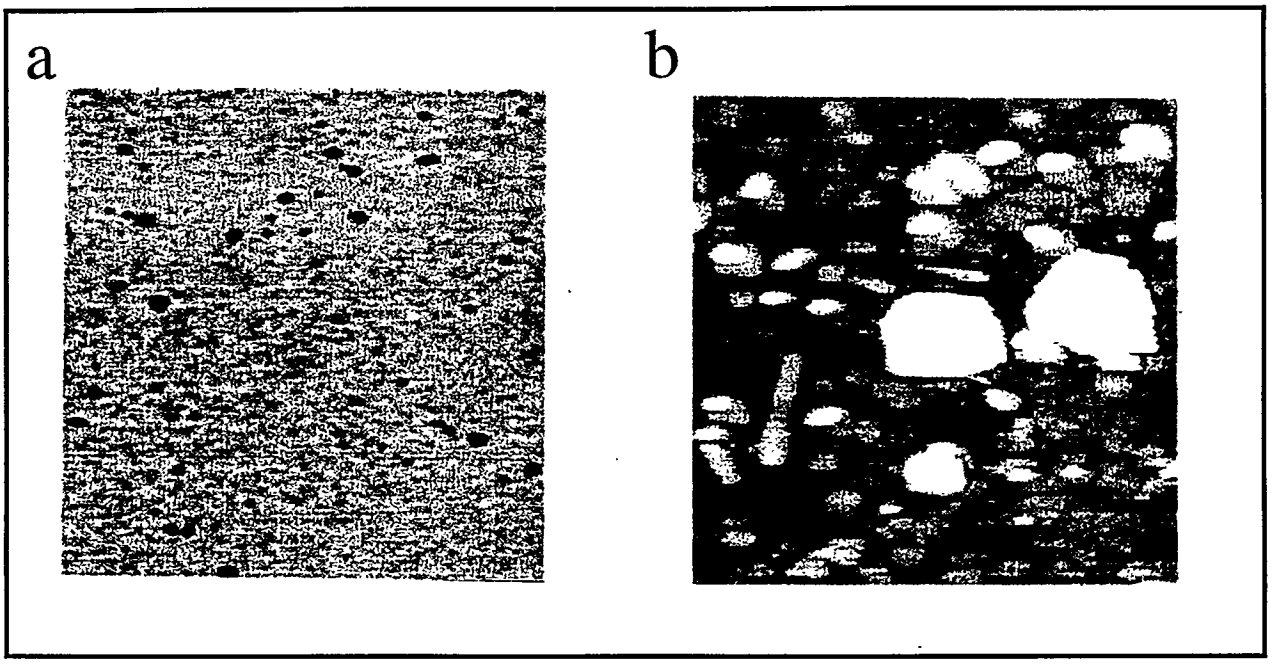

Fig. 2. a) 1 μm AFM image of a YSZ buffer layer on Si showing pinholes (from ref. 13). b) 1 μm AFM image of completed YBCO/YSZ buffer layer.

J_c(4 K) = 10^7 A/cm^2. An AFM image of the YBCO/YSZ bilayer is shown in Fig.2b. Large ablation boulders dominate the image. Between the boulders the film appears flat (roughness less than 10 nm) indicating predominate c-axis growth. We estimate the c-axis grain size to be 90 to 100 nm based on the average distance between roughness peaks. A few long, narrow a-axis grains are also present along with some round protrusions, 50 to 60 nm high and 150 nm in diameter. The density of the round protrusions is about 30/μm^2 which is close to the YSZ pinhole density derived from Fig. 1 of 50/μm^2. We submit that there may be a correlation between the round protrusions and the YSZ pinholes and that they may well be evidence of reaction between the YBCO and the Si.

SCANNING POTENTIOMETRY OF YBCO STEP EDGE JUNCTIONS

The AFM has been adapted for scanning potentiometry.[6] The main features of the modifications to the AFM include a laser beam bounce technique for measuring the deflection of the cantilever which is excited near its resonance frequency by ac capacitive forces between the tip and the sample. The resonant force is minimized by adjusting the dc voltage between the tip and the sample to be the same. This voltage adjustment is plotted as a function of x-y position giving a potential map of the surface. This technique is useful for measuring surface potential due to changes in work function, trapped charges, or current flowing through a device such as a contact via or along an interconnect with 50 nm spatial resolution and millivolt voltage resolution.

We have performed some tests at room temperature on step edge structures for superconductor-normal metal-superconductor (SNS) proximity effect devices. Here, YBCO is deposited at an angle over a previously ion milled step forming a break in the film. Au is then deposited from the other side completing

the junction. Most of the gold is ion milled away leaving a small amount between the banks of the YBCO films on either side of the step forming the junction.

Figure 3a shows the surface potential image of a step-edge junction energized with 10 mA. The corresponding topography is shown in Fig. 3b. Line scans as a function of position across the junction are shown in Fig.s 3b and 3c. The data shows a linear dependence of voltage along the line as expected. Also, a dip in the surface potential at the junction as well as peaks in the surface potential near laser ablation boulders can be seen in the potential images. As mentioned above the technique is sensitive to surface charging which may be the explanation for the dip near the junction. Charge accumulation at the bare interface may have an effect on the operation of these HTS devices.

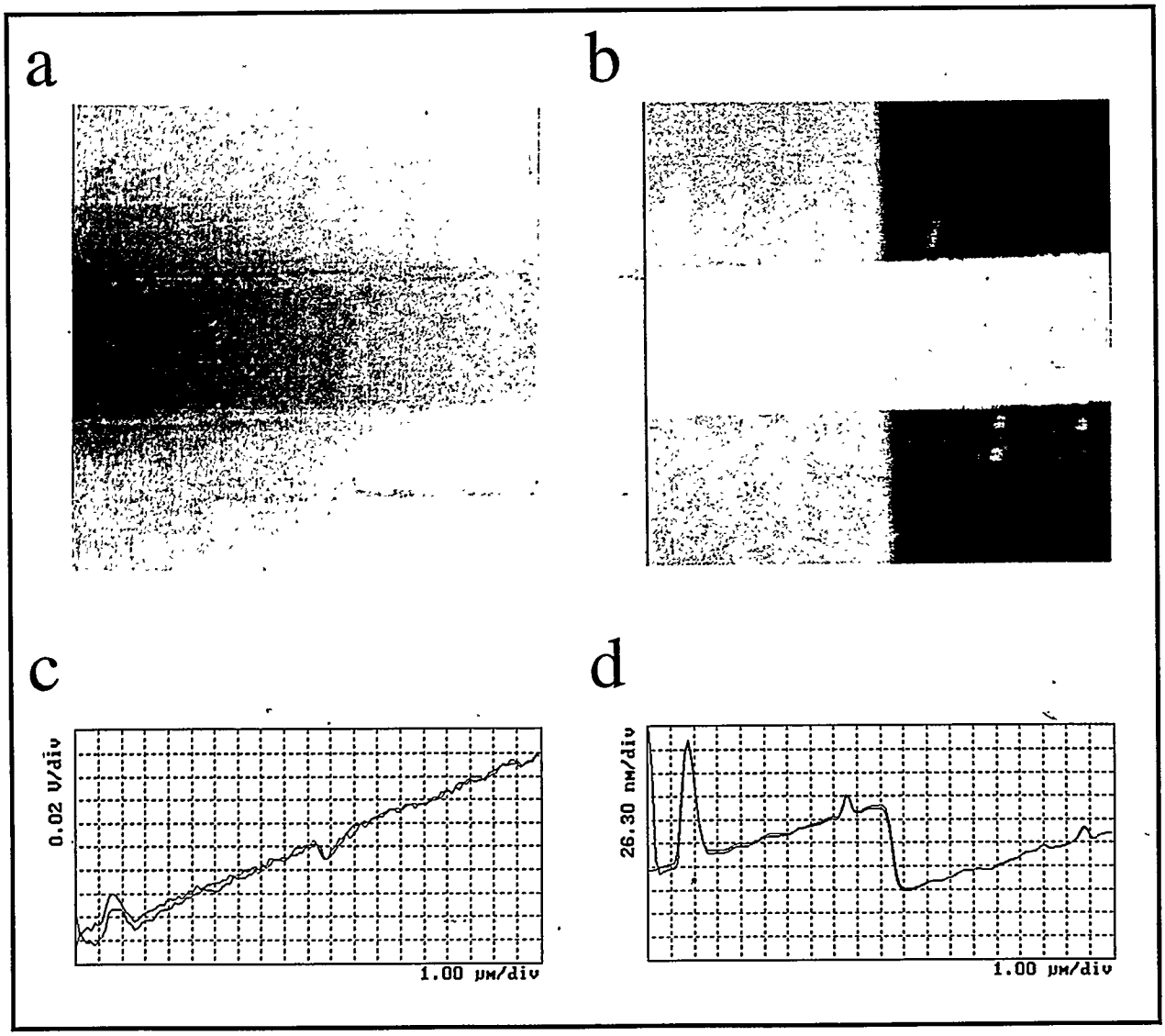

Fig. 3 a) Surface potential image of a YBCO step-edge junction at room temperature. b) Corresponding AFM topography for Fig. 3a. c) Line trace of surface potential vs distance across YBCO step-edge. d) Line trace of the z-height vs distance across the YBCO step-edge.

SUMMARY

In summary, we have shown that STM can be used to image differences in the grain morphology of as-grown, *in situ* YBCO films deposited on various substrates by sputtering or laser ablation. The newly developed long scanning range capabilities combined with the exquisite vertical sensitivity make the STM unique for this type of application. The images are useful for determining the growth habit on individual grains and may be helpful in determining grain boundary structures. We have also looked at STM images of sputtered YBCO films at various temperatures. The images show anomalously large step corrugation at room temperature compared to the expected unit cell step of 1.2 nm. The STM step height is temperature dependent, however, decreasing to close to the expected value at 76 K. Preliminary speculations about the cause of this phenomenon include the possible presence of a semiconducting layer at the surface of the film that undergoes carrier freeze-out or the inception of 2D localization of electrons within CuO planes at lower temperatures. In any case, the tunneling characteristics that effect the STM image are important for understanding the electrical properties of the surfaces of YBCO films. Such information is needed for development of Josephson tunneling barriers and electrical interconnect structures that would be useful for scaleable integrated circuit applications.

The nature and chemical composition of the sand particles are at this time unknown. They may stem from slight variations in YBCO stoichiometry. They are always present in high quality YBCO films made under a variety of deposition conditions. YBCO sand may have significant consequences for multilayer structures being considered in interconnect technologies. If these particles are distributed evenly throughout YBCO films they may occur at high enough volume densities to account for high J_c pinning in YBCO films.

AFM images of YSZ/YBCO bilayers on Si indicate the presence of pinholes in the YSZ layer bridging the Si and the YBCO. This leads to the subsequent formation of nonconducting phases near the pinholes since YBCO and Si react during high temperature processing steps. AFM images show scattered mounds on the completed YSZ/YBCO bilayers having about the same surface density as that of the pinholes. In the future we hope to apply the information gained from STM and AFM to optimize the transport properties of narrow superconducting YBCO lines on Si. Preliminary results show that it is possible make 0.25 μm lines which appear to be largely unharmed by e-beam lithography and subsequent ion milling.

AFM potentiometry based on the force-null detection scheme described above should be useful for studies of microelectronic devices offering better than 100 nm lateral resolution and better than 1 mV voltage resolution. Force-detection scanning potentiometers are sensitive to charging effects. We are developing a simple image subtraction process to minimize the effects of charging.. In addition, we have observed various charging affects including transfer of charge between the AFM tip and the sample. We have also observed switching of the charge state of the AFM cantilever between quasi-stable levels. Oxides on or near the surface of the tip may be responsible. Also, the tip may be picking up charged particles from the sample surface. Several labs have been experimenting with high bandwidth scanning potentiometry of semiconducting devices at frequencies as high as 100 GHz.[15,16,17] Ultimately our goal is to extend their work to low temperature studies of active HTS devices .

NEW DIRECTIONS: MAGNETIC RESONANCE IMAGING AT THE NANOMETER SCALE

Magnetic resonance imaging (MRI) which has the advantages of being non-destructive, chemically specific, and three-dimensional but it is unfortunately limited to the 10 μm spatial resolution level.[18] This barely qualifies MRI as a microscopic technique. Conventional MRI resolution is limited by relatively weak field gradients of order 10^{-1} T/m and the signal-to-noise ratio of the standard pick-up coil circuits

used to detect selected spins. Scanned probe microscopies (SPM), on the other hand, have high resolution, but only probe on or above surface structures. An example is magnetic force microscopy (MFM) which is a well developed SPM technique currently in use by the magnetic data storage industry. MFM routinely gives 50 nm spatial resolution images of the average fields above the surfaces of disk drive components. A new type of SPM related to MFM and referred to as magnetic resonance force microscopy (MRFM) has the main advantages of MRI of being chemically specific, three dimensional, and non-destructive in addition to the high resolution of SPM. MRFM was first proposed by Sidles.[19] It has the potential to greatly improve the current imaging technology for investigations of magnetic resonance phenomena down to the atomic scale.

In MRFM, a force microscope cantilever is used to detect the magnetic force exerted when spins are brought into resonance in response to an applied rf field. In theory, it has the sensitivity required to detect a single nuclear spin by exploiting the very large (~10^8 T/m) field gradient near a sharp magnetized tip similar to those used in MFM. In contrast to MRI, the large field gradients that produce the high spatial resolution also increase the intensity of the magnetic coupling signal between the cantilever and each individual spin residing in the selected slice. This combination is key to overcoming the resolution limits of conventional MRI. Additionally, the scanned probe used in MRFM simplifies the image reconstruction process normally required for conventional MRI.

MRFM differs from other types of SPM in its ability to probe sub-surface structure. Resonant coupling occurs when the Larmor condition is satisfied a points which lie on a surface *remote* from the tip of the probe where the magnetic field is at the appropriate value. This gives MRFM sub-surface sensitivity and a slice selectivity like that in conventional MRI experiments. Additionall, as in conventional magnetic resonance experiments, the spin precession frequency varies for different nuclei or compounds, thus giving MRFM its chemical specificity.

The general operating principles of MRFM are as follows: The spins in the sample are polarized by the magnetic field from the MFM tip, which, as discussed above, also produces the field gradients needed to generate a measurable magnetic force on the cantilever and provide spatial resolution for imaging. The spins in the sample are then resonantly excited by an applied rf field that is modulated at the resonant frequency of the cantilever which producing vibrational motion of the cantilever. Magnetic force maps are produced by measuring the vibrations of the cantilever attached to the sample while scanning the tip with respect to the sample. Real-space imaging information can be recovered from the force maps by using the usual deconvolution image reconstruction methods. The principles of MRFM have been demonstrated by Rugar, *et.al.*[20]. Their prototype microscope has achieved 1 μm resolution, which is 10 to 100 times better than conventional MRI instruments tailored for microscopy of small samples. While 1 μm resolution is far from the 10 pm resolution predicted by theory, the apparatus is relatively crude and not near the current limits of existing technology.

ACKNOWLEDGMENT

The author acknowledges the contributions of R. E. Thomson, R. H. Ono, A. Roshko, S. E. Russek, T. E. Harvey, J.W. Ekin D. A. Rudman, A. J. Nelson, B. Jeanneret, S. C. Sanders, P. Rice and C. Prater. JM was supported by DoE BES contract DE-AIO5-89ER14044

REFERENCES

1. E. M. AJIMINE, F. E. PAGADUAN, M. M. RAHMAN, C. Y. YANG, H. INOKAWA, AND D. E. FORK, AND T. E. GEBALLE, "Electrical Characterization Of Metal-Insulator-Semiconductor Diodes Fabricated From Laser Ablated $YBa_2Cu_3O_x$ /Yttria Stabilized Zirconia Films On Si Substrates," *Appl. Phys. Lett.* 59 , 2889 (1991).
2. T. E. HARVEY, J. MORELAND, B. JEANNERET, R. H. ONO, AND D. A. RUDMAN, "$YBa_2Cu_3O_x$ To Si Interconnection For Semiconductor/Superconductor Integration," *Appl. Phys. Lett.* 61, 225 (1992).
3. see this proceedings
4. H. J. GUNTHERODT AND R. WIESENDANGER, *Scanning Tunneling Microscopy,* Springer Verlag, New York, Springer Series on Surface Science vol.s 20, 28, and 29 (1994).
5. DROR SARID, *Scanning Force Microscopy*, Oxford, New York (1994).
6. Y. MARTIN, D. W. ABRAHAM, H. K. WICKRAMSINGHE, "High Resolution Capacitance Measurement And Potententiometrie By Force Microscopy," *Appl. Phys. Lett.* 52, 1103 (1988).
7. D. P. NORTON, D. H. LOWNDES, X. -Y. ZHENG, S ZHU, AND R. J. WARMACK, *Phys. Rev. B* 44, 9760 (1991).
8. I. D. RAISTRICK, M, HAWLEY, J. G. BEERY, F. H. GARZON, AND R. J. HOULTON, *Appl. Phys. Lett.* 59, 3177 (1991).
9. JOHN MORELAND, PAUL, RICE, S. E. RUSSEK, B. JEANNERET, A. ROSHKO, R. H. ONO, AND D. A. RUDMAN, "Scanning Tunneling Microscopy. Of The Surface Morphology Of $YBa_2Cu_3O_x$ Thin-Films Between 300 K And 76 K," *Appl. Phys. Lett.* 59, 3039 (1991).
10. M. HAWLEY, I. D. RAISTRICK, J. G. BERRY, AND R. J. HOULTON, "Growth Mechnism Of Sputtered Films Of YBCO Studied By Scanning Tunneling Microscopy," *Science* 251 , 1587 (1991).
11. R. E. THOMSON, J. MORELAND, N. MISSERT, D. A. RUDMAN, AND S. C. SANDERS, "Insulating Nanoparticles On $YBa_2Cu_3O_x$ Thin Films Revealed By Comparison Of Atomic Force And Scanning Tunneling Microscopy," *Appl. Phys. Lett.* 63, 614 (1993).
12. private communication J. Mannhart, University of Basel, Switzerland.
13. J. MORELAND, T. E. HARVEY, R. H. ONO, AND A. ROSHKO, "Scanned Probe Microscopy Of $YBa_2Cu_3O_x$ Thin-Film Device Structures On Si Substrates", *IEEE Trans. on Appl. Supercon.* 3, 1586 (1993).
14. D. K. FORK, D. B. FENNER, R. W. BARTON J. M. PHILLIPS, G.A.N. CONELL, J. B. BOYCE, AND T. H. GEBALLE, "High Critical Currents In Strained Epitaxial YBCO On Si", *Appl. Phys. Lett.* 57, 1161 (1990)
15. H. YOKOYAMA, T. INOUE, AND J. ITOH, "Nonresonant Detection Of Electric Force Gradients By Dynamic Force Microscopy, *Appl. Phys. Lett.* 65, 3143, (1994).
16. A. S. HOU, F. HO, AND D. M. BLOOM, "Picosecond Electrical Sampling Using A Scanning Force Microscope," *Electronics Lett.* 28, 2302 (1992).
17. C. BOHM, C. ROTHS, AND E. KUBALEK, "Scanning Force Microscope Test System For Internal Test With High Spatial And Temporal Resolution", *Microelectronic Engineering*, 24 91 (1994).
18. P. T. CALLAGHAN, *Principles Of Nuclear Magnetic Resonance Microscopy*, Oxford, New York, (1991).
19. J. A. SIDLES, "Noninductive Detection Of Single Proton Resonance", *Appl. Phys. Lett.* 58, 2854 (1991).
20. D. RUGAR, C. S. YANNONI, AND J. A. SIDLES, "Mechanical Detection Of Magnetic Resonance", *Nature* 360, 563 (1992).

PROTECTION OF HIGH TEMPERATURE SUPERCONDUCTING THIN-FILMS IN A SEMICONDUCTOR PROCESSING ENVIRONMENT

Yizi Xu, Richard Fiske, S.C. Sanders, and J.W.Ekin

Electromagnetic Technology Division
National Institute of Standards and Technology
Boulder, CO 80303, U.S.A.

ABSTRACT

Annealing studies have been carried out for high temperature superconductor $YBaCuO_{7-\delta}$ in a reducing ambient, in order to identify insulator layer(s) that will effectively protect the superconducting film in the hostile environment. While a layer of magnesium oxide (MgO) sputter deposited directly on $YBaCuO_{7-\delta}$ film provides some degree of protection, we found that a composite structure of YBCO/$SrTiO_3$/MgO, where the $SrTiO_3$ was grown by laser ablation immediately following YBCO deposition (in-situ process), was much more effective. We also address the need for a buffer layer between YBCO and aluminum (Al) during annealing. Al is most commenly used for semiconductor metalization, but is known to react readily with YBCO at elevated temperatures. We found that the most effective buffer layers are platinum (Pt) and gold/platinum (Au/Pt).

INTRODUCTION

Recently there have been several demonstrations of potential applications of superconductor-semiconductor integrated systems. One example is microwave filter subsystem made with high-temperature-superconductor (HTS) yttrium-barium-copper-oxide (YBCO) that can be used in cellular base stations[1]. Combined with cryogenic low-noise amplifiers (made from semiconductors), these compact HTS receiver filter subsystems provide much improved noise/interference rejection and hence higher service quality, more usable channels, and an extended coverage area. Another example of significant potential benefits of superconductor-semiconductor integration technology is the sensor subsystem used in magnetic resonance imaging (MRI) systems[2], currently the biggest commercial market for superconducting technology. The growing interest in low-cost, low-field MRI has created a challenge in MRI sensor technology that can only be met with the development of HTS-based low-noise receiver coils and their successful integration with low-noise semiconductor amplifiers operated at cryogenic temperatures.

The superconductor-semiconductor integration may be achieved in different levels, dependent upon particular applications[3]. At the system and subsystem level, semiconductor wafers are combined with chips carrying superconductor circuits, with each fabricated and processed separately under conditions that are optimized for each of them. This is the approach being followed now in the microwave filter applications. The next step of hybridization involves growing semiconductor and superconductor devices and circuits on the same wafer. More fundamental compatibility issues arise in this step, and it is with some of these issues we will be concerned in this work.

As an example consider the metalization and contact formation process. Aluminum is the most commonly used for metalization and interconnection in semiconductor integrated circuits. A process called contact sintering (or contact alloying) is used to form a reliable and intimate Al/Si

contact. This involves annealing the contact at temperatures close to 400 °C and in a reducing ambient, provided by the "forming gas", which is a mixture of 5-10% at. hydrogen and 95-90% at. nitrogen [4]. This typical semiconductor process will, however, seriously degrade the quality of YBCO film. The properties of HTS YBCO, such as T_c and the critical current density J_c, depends critically on its oxygen stoichiometry, which is readily depleted in such a process. Moreover, aluminum is known to react with YBCO at elevated temperatures by removing oxygen from the latter, thus compounding the problem of oxygen loss. Proper procedures must be taken to protect the YBCO circuits if the YBCO/Si hybrid at the chip level is to fit into the existing, well established semiconductor processing technology.

We have taken a two-step approach to identify these procedures. First we investigate noble metals that can serve as a buffer layer between YBCO and Al during annealing in oxygen atmosphere. The reason for using oxygen instead of forming gas, for example, is to differentiate the effects due to aluminum diffusion into and interact with YBCO, from that due to pure oxygen loss from the YBCO. Second we investigate insulating/dielectric materials that can be used to cover YBCO during argon gas annealing, to prevent oxygen out-diffusion due to the reducing ambient.

EXPERIMENTAL

Buffer Layer For Aluminum Diffusion During Oxygen Annealing

The HTS YBCO films used for aluminum diffusion buffer study were grown on (100) oriented MgO substrates using pulsed laser deposition. Briefly, the MgO substrate was heated to 730 °C, and a laser beam (wavelength=248 nm) with fluence of 2 mJ/cm^2 was focused at a target which was about 9 cm away from the substrate. The pulse rate was 10 pulses/sec and a total of 10,000 pulses gave a nominal thickness of 200 nm. The oxygen background pressure was 27 Pa (200 mTorr) during the deposition, and was brought to 500 Torr during cooling down after deposition. The YBCO films were predominantly c-axis oriented with a high degree of in-plane epitaxy, as revealed by x-ray diffraction. Critical temperatures were in the range of 85–90 K, and the J_c's were typically in excess of 10^6 A/cm^2 at 77 K.

Noble metal buffer layers were deposited on top of YBCO *in situ* (i.e., without breaking the vacuum) by either magnetron sputtering or thermal evaporation, immediately followed by deposition of a top layer of Al, using thermal evaporation. Unless otherwise stated, the Al, as well as each metal layer composing the buffer structure, was 50 nm thick.

The resistance-versus-temperature (R vs. T) measurements were taken in a standard four-probe configuration. The T_c was determined as the temperature at which the sample resistance dropped to 10% of the value at the onset of the transition.

The upper panel of Fig.1 shows the results of 300°C annealing in oxygen for different buffer layers. Buffer layers consisting of Au, Au/Cr, and Au/Ag resulted in the loss of superconductivity down to 76K. The Ag buffer layer was somewhat more effective, but showed a steady and significant decrease of T_c with annealing time. The buffer layers consisting of Pt or Au/Pt were the most effective as barriers for aluminum diffusion. In both cases, there was an increase in T_c after the first 30 minutes of annealing, possibly due to the ordering of initially disordered oxygen atoms on the Cu-O chain sites at this temperature. We also note that there was very little change in T_c beyond the initial 30 minutes, for times up to 2.5 hours.

Encouraged by these results, we raised oxygen annealing temperature to 400°C for samples having Pt and Au/Pt buffers. The results are shown in the lower panel of Fig.1. They are very similar to those displayed in the upper panel. However, 400°C is a typical temperature used in contact alloying in semiconductor process, therefore the significance of this result is that we have identified buffer layers to protect YBCO from aluminum diffusion that are effective at semiconductor processing temperatures.

We now turn to the second step, i.e., to replace the oxygenating ambient with a reducing ambient, e.g., argon, which is actually used in semiconductor contact alloying.

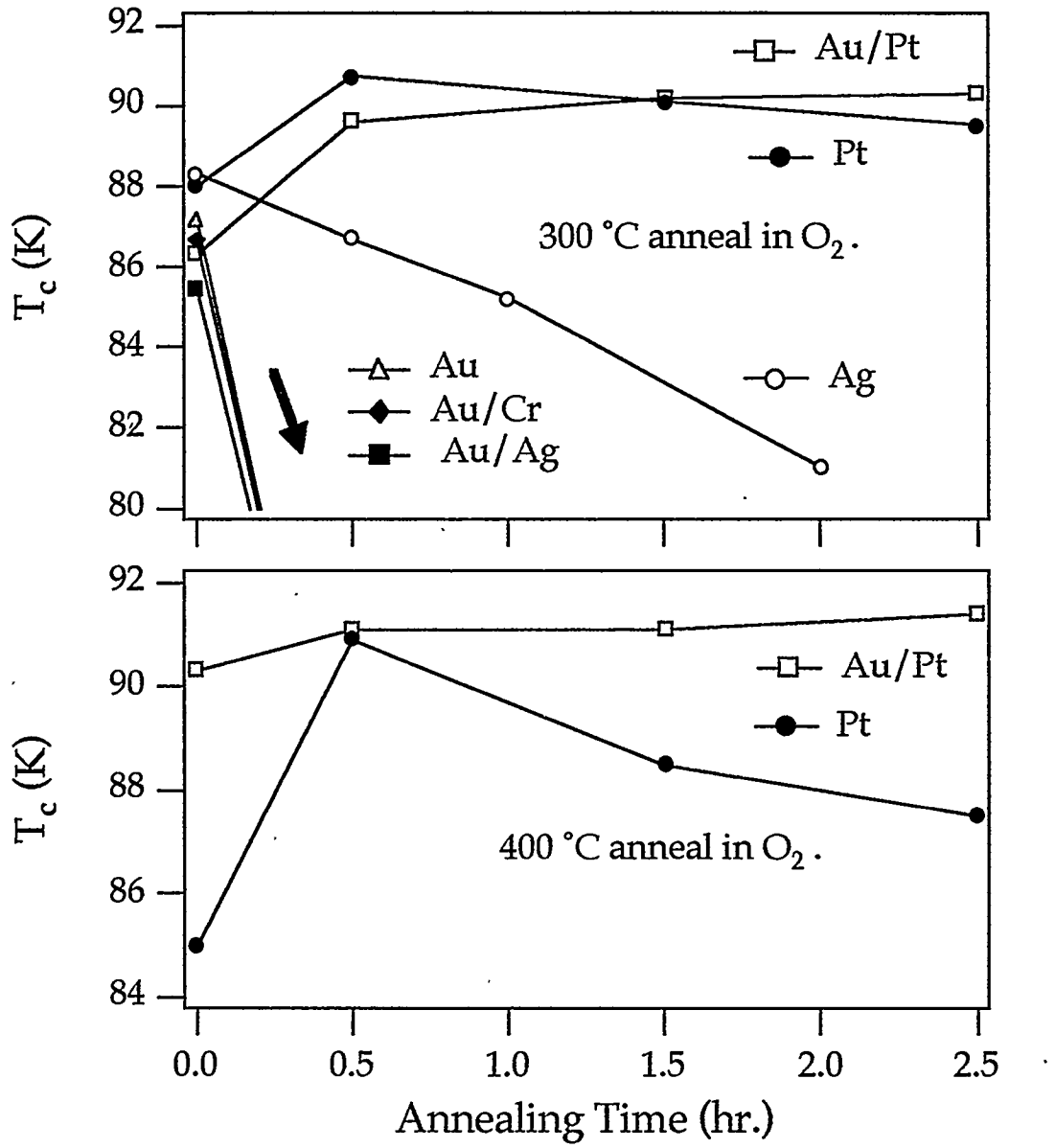

Fig. 1 T_c vs. annealing time of YBCO/buffer/aluminum structure for a number of buffer layers annealed in O_2. The buffer layers made of Au/Pt and Pt were the most effective.

Insulating Layer For Protection of YBCO During Argon Annealing

Here we focus on insulating materials, instead of noble metals, that will protect YBCO during annealing in argon gas. The candidate material we chose was magnesium oxide (MgO) grown by magnetron sputtering.

We have used two types of films in this study. The first type is a bare YBCO film, of 200 nm nominal thickness, on $LaAlO_3$ substrates. The second type, has an overlayer of 30 nm $SrTiO_3$ (STO) deposited *in situ* on top of the 200 nm YBCO film. The purpose of this overlayer is to passivate the YBCO surface thereby preventing oxygen loss during subsequent processing and handling. Both types of films were coated with an MgO layer with a nominal thickness of 75 nm prior to annealing, as depicted in figures 2(a) and 2(b).

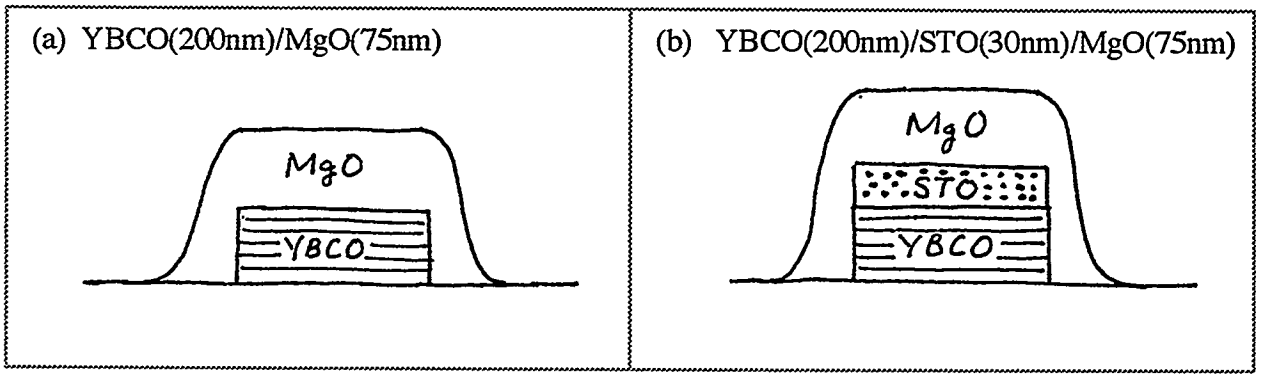

Fig. 2(a) Cross-section of structure A: YBCO film coated with sputter deposited MgO layer.

Fig. 2(b) Cross-section of structure B: YBCO film with a (*in-situ*) STO overlayer, coated with an MgO layer.

Figures 3(a) and 3(b) compare the effects of annealing on these two types of films. The annealing was carried out in a bench top annealing furnace. The gas used was a mixture of 5 % at. hydrogen and 95% at. argon, simulating the "forming gas", and the duration was 20 minutes at 400°C. The T_c measurement was done using an inductive, non-contact technique.

Fig. 3(a) is for a film of bare YBCO coated with 75 nm of MgO. The T_c of the YBCO film was 85.5 K before annealing. It dropped to 47 K after annealing, presumably due to extensive oxygen loss. This is a clear indication that MgO layer alone is not adequate.

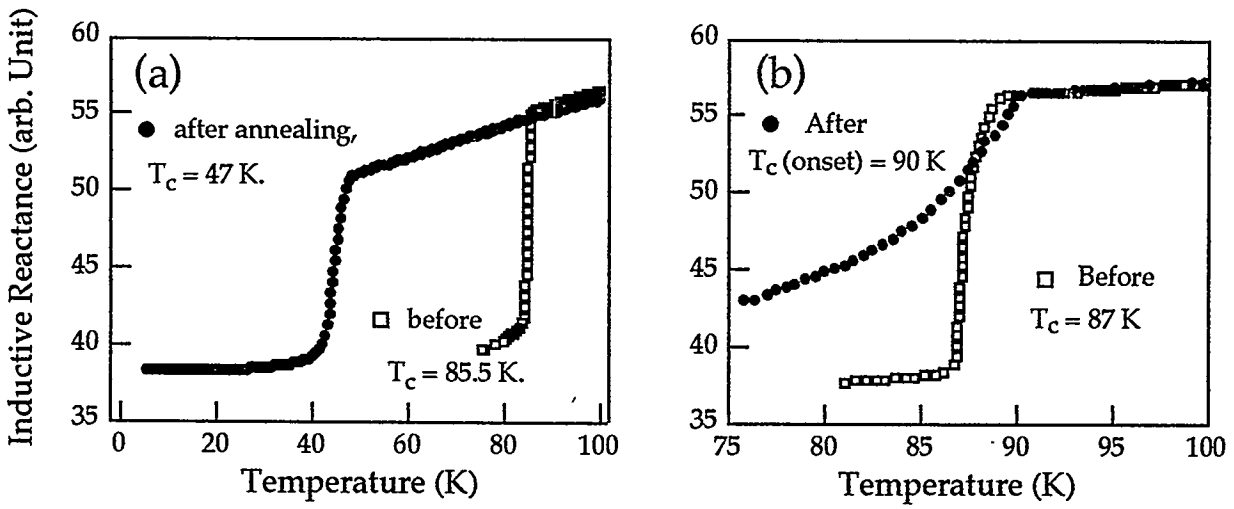

Fig.3 Inductive T_c measurement of unpatterned YBCO films. (a) YBCO(200nm) /MgO(75nm); (b) YBCO(200nm)/STO(30nm)/MgO(75nm). Anneal conditions: 20 mins. @ 400 °C in Ar_2 (95%) + H_2 (5%).

Fig. 3(b) is for a YBCO film with 30 nm STO overlayer. In contrast to the film with MgO layer alone, the onset of the superconducting transition of this film after annealing, close to 90 K, was actually higher than its pre-annealing value. We note that, unlike transport measurement, in the case of inductive measurement the onset of the transition actually signals that a large volume fraction of the sample had become superconducting. This result was the first evidence that a combined structure of STO/MgO could be effectively used to protect YBCO film during forming-gas annealing. However, we also note that was a long tail to the transition, and its depth did not reach the pre-annealing magnitude even at 76 K, indicating a non-uniform distribution of superconductive transitions within the film.

We also patterned several films for transport measurements, in order to compare with the inductive measurements. The pattern consists of a 20 μm wide line with voltage taps 2 mm apart. Four-point resistance was measured using an ac technique with a lock-in amplifier. These films were annealed in a tube furnace in flowing Ar_2, with no hydrogen.

Fig. 4 shows the resistivity versus temperature behavior for a patterned film of the type YBCO(200nm)/ STO(30nm). Before annealing, the resistivity just above the transition is only about 70 μΩ•cm. At 77 K the critical current density J_c was 3.5×10^6 A/cm^2. The film was annealed in a tube furnace at 400 °C in flowing Ar_2 for 20 minutes. We note that after annealing the resistivity just above the transition was nearly doubled, indicating degraded normal state transport properties. The change in the superconducting state was more interesting. The bulk of the transition was 91 K, up by 4 K from the pre-anneal value. However, the film was not fully superconducting even at 77K. The resistance remained finite, at about 10% of its value at the onset of the transition, and showed little temperature dependence thereafter.

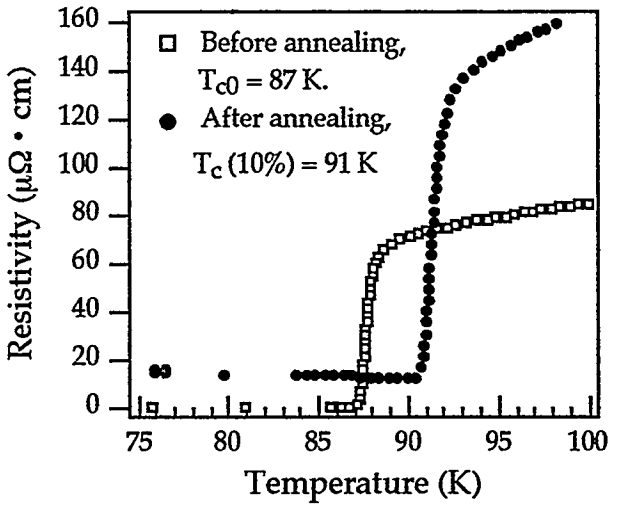

Fig. 4 Resistivity vs. temperature of a patterned YBCO/STO film coated with 75 nm of MgO, before and after Ar_2 anneal.

This result is consistent with that of the inductive measurement (cf. Fig.3(b)). The annealing in argon gas environment increased the transition temperature in the bulk of the YBCO film. It had also created a "foot" in the superconducting transition, which may be associated with localized regions having severe oxygen deficiency. The formation of these regions may conceivably be attributed to oxygen loss through the STO/MgO structure, possibly through pinholes in the MgO, which provided passageways for oxygen out-diffusion during annealing.

To proceed further we modified the MgO deposition procedure. Instead of finishing it in a single vacuum run, we did two sequential runs. We removed the chip from the chamber after the first run, leaving it in the air overnight and then loaded it back to the vacuum chamber for the second run. The total time was kept the same so that the total MgO thickness was the same. However, due to the air exposure, the locations of pinholes in the second MgO layer may not align exactly with those formed in the first MgO layer. This method may therefore enable us to get around the difficulty of pinholes in MgO.

Fig. 5 shows our best result so far. The film was YBCO(200nm)/STO(30nm) type, and was patterned for transport measurement. Before annealing, the room temperature resistivity was about 340 μΩ•cm, and J_c (77K) ~ 3.0×10^6 A/cm^2. After these initial measurements the film was coated with 75 nm of MgO using the two-step sequential deposition procedure, followed by annealing in

flowing argon gas for 20 minutes at 400 °C. We note that the film normal state resistivity increased only slightly after annealing. Moreover, the superconducting transition temperature, T_{c0}, increased from 87.5 K to 88.5 K. In addition the critical current density remained quite high: J_c (77K) ~ 2.0×10^6 A/cm^2. This result demonstrates that YBCO films, protected by an *in-situ* overlayer of STO and sequentially deposited MgO double layers, is capable of withstanding annealing in forming-gas, for temperatures and durations typically found in semiconductor processing. T_{c0} tends to increase slightly, and J_c degradation was small.

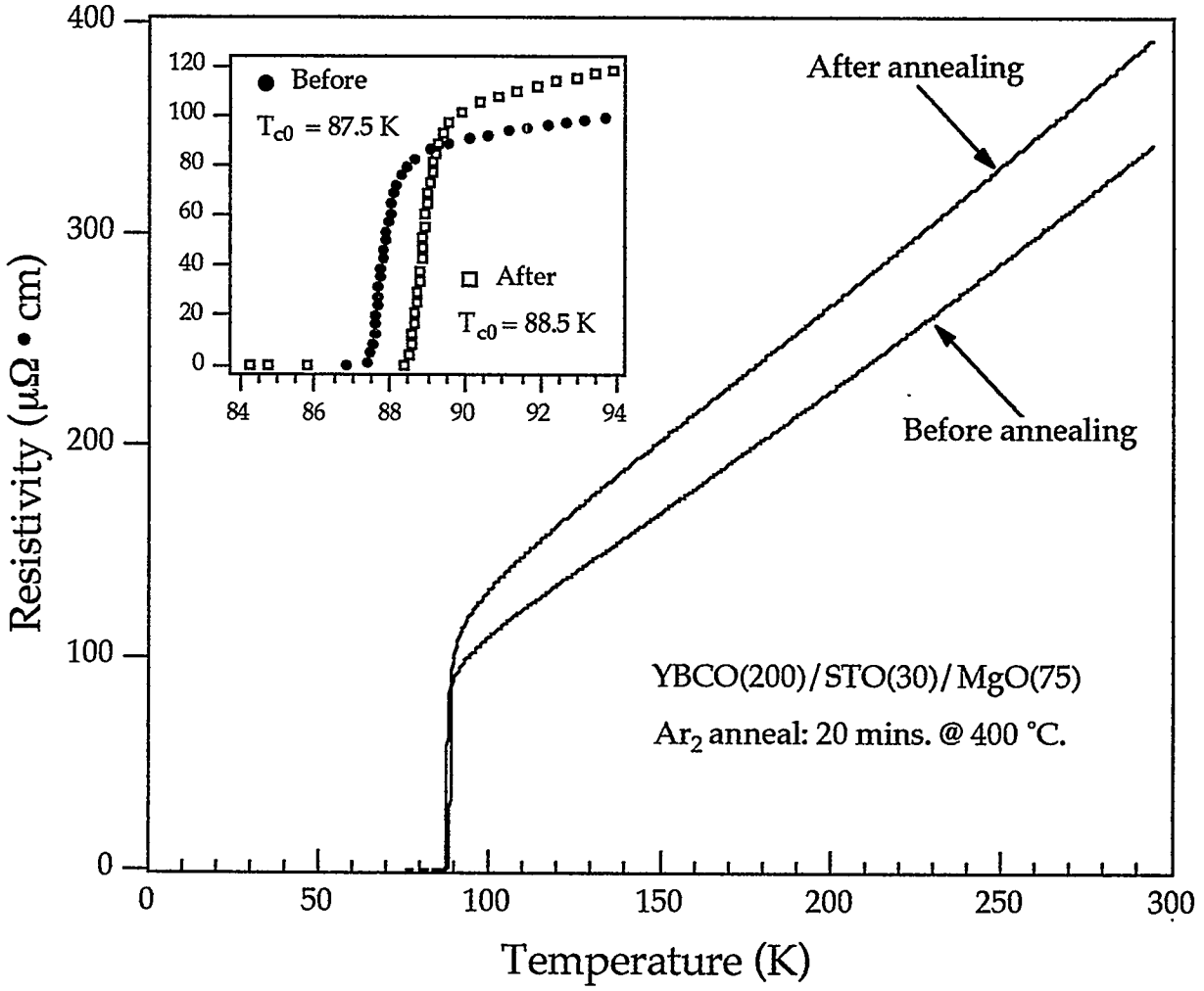

Fig. 5 Resistivity vs. temperature of a patterned YBCO/STO film before and after Ar_2 anneal. The MgO protection layer was grown using a modified 2-step sequential sputter deposition process, see text for details.

The importance of the STO *in-situ* overlayer can be readily appreciated by comparing Fig. 5 with Fig. 6, which displays the annealing results of another YBCO film. This film was without a STO overlayer, but went through the same procedure as the sample in Fig. 5, i.e., a two-step sequential coating of MgO, followed by annealing in argon at 400 °C for 20 minutes.

We note that both the normal state behavior, as well as the superconducting properties changed markedly. T_{c0} decreased from ~ 88 K to 79 K, just above the liquid nitrogen boiling temperature. Moreover, J_c (77K) decreased form ~2.5×10^6 A/cm^2 to a mere 3.5×10^3 A/cm^2, a nearly ten-fold reduction. This result clearly demonstrates the importance of an overlayer with high crystalline quality.

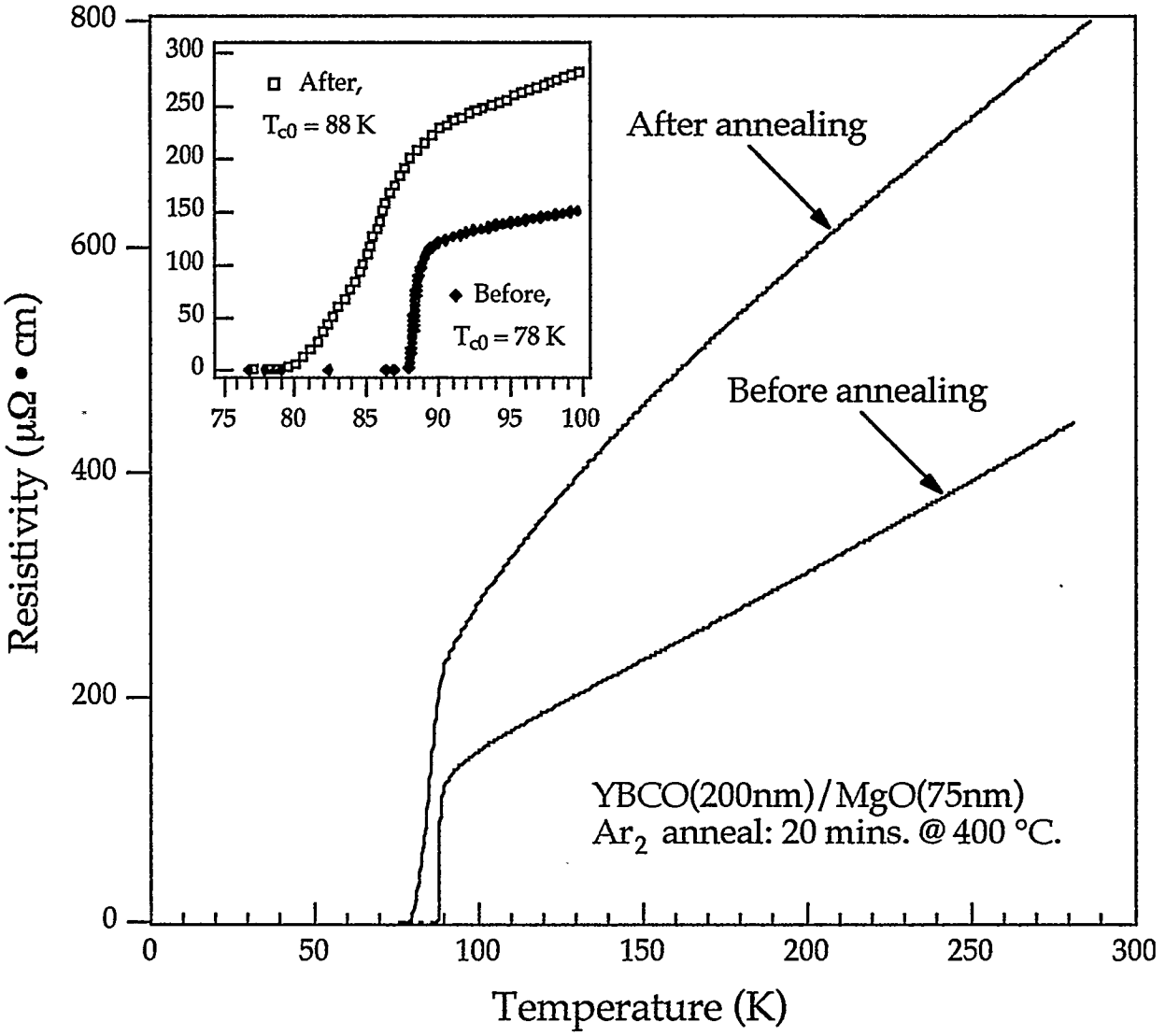

Fig. 6 Resistivity vs. temperature of a patterned YBCO film before and after Ar_2 anneal. The MgO protection layer was grown using a modified 2-step sequential sputter deposition process, see text for details.

The Effect Of Annealing Temperature

We also studied the influence of the annealing temperature. Two more chips, one is identical to that of Fig. 5 (identical in the sense that they were diced from same wafer), and the other identical to that in Fig. 6, were annealed in argon gas at 450 °C for 20 mins. The results are shown in figures 7 and 8. Neither was superconducting at 77 K after annealing. However, less damage was done to the film with STO overlayer: its T_{c0} was 60 K, about 10 degrees higher than the one without STO overlayer, and the increase in the normal state resistivity was several times smaller.

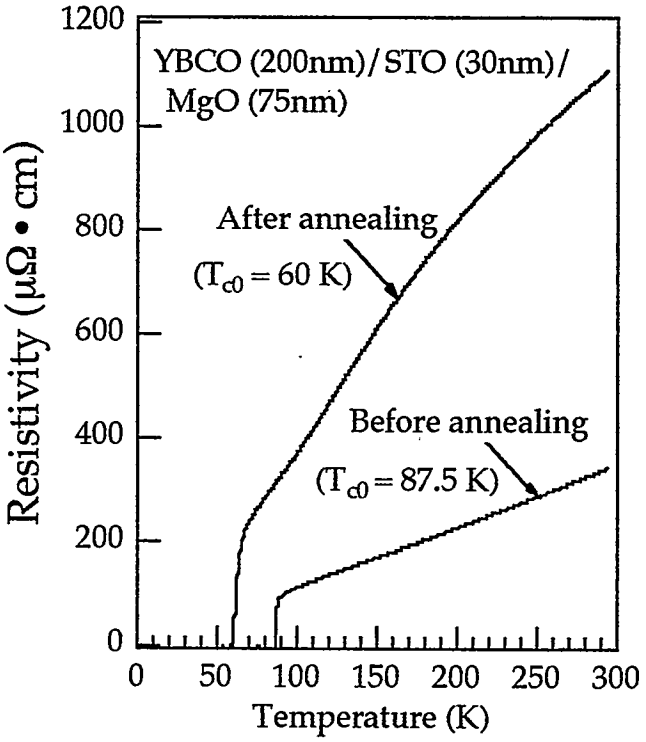

Fig. 7 R vs. T before and after annealing of a patterned film of YBCO/STO. It was covered with a 75 nm MgO using a 2-step sequential deposition process. Ar_2 anneal was at 450 °C for 20 minutes.

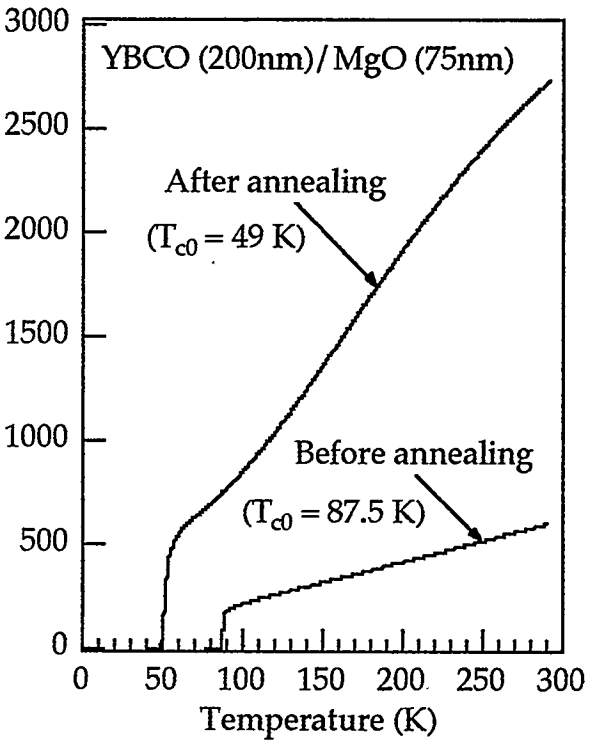

Fig. 8 Similar to Fig. 7, except that the YBCO film did not have STO overlayer.

DISCUSSION

We summarize here systematic trends observed in our Ar_2 gas annealing studies.

First, Ar_2 annealing general degraded the superconducting and normal state properties of YBCO films, the extent depends strongly on the annealing temperature, the structure of the protection layer, and the procedures with which these structures were made. The cause is almost certainly the oxygen out-diffusion, which should have a strong temperature dependence. This is supported by the results shown in figures 5, 6 and figures 7, 8. A mere 50 °C increase in annealing temperature the had resulted in much more extensive loss of oxygen.

Second, it is known that oxygen diffusion is highly anisotropic in YBCO crystals, with the rate in ab-plain being much higher than that along c-axis direction[5]. In thin films the anisotropy may not be as great, due to defects assisted hopping along the c-axis direction. We believe that in our films diffusion in both directions are taking place and are perhaps equally important. For a patterned film such as our J_c test structure, oxygen out diffusion could proceed either along the c-axis direction, which is perpendicular to the film, or in the ab-plain to exit through the edges of the patterned line. However, as long as the annealing temperature is not too high (e.g., less than 400 °C in our experiments), the diffusion rate in neither direction is high, the oxygen loss through the edge diffusion is limited to the periphery of the line. Consequently the annealing results is determined essentially by the perpendicular diffusion, since the films are much thinner than they are wide (0.2 μm vs. 20 μm). This may explain the beneficial effects of the STO overlayer, which is primarily effective in hindering oxygen out-diffusion in the perpendicular direction.

Third, it is also well documented that oxygens on the CuO chain sites in YBCO can be easily displaced under influences of moderate thermal, electrical (e.g., electromigration current[6]) and structural (e.g., strain at high-angle grain boundaries) disturbances. However, the thermally driven oxygen displacement, as in the case of electrically driven oxygen defects migration (electromigration), can have rather different effects on YBCO properties depending on the magnitude of the driving force. A small driving will usually have some beneficial effects due to oxygen reordering. Examples of this are the noticeable increase in the onset of the superconducting transition in Fig.4, and the increase in T_{c0} in Fig. 5. These are not likely due to the increase in oxygen content in the film during annealing, since it was carried out in reducing ambient. Rather, they are due to the improved oxygen vacancy ordering in the interior of the line. Under a larger driving force, rapid and long-range oxygen diffusion occurs, leading to extensive loss of oxygen (mostly through the edge of the patterned lines), and drastic deterioration in film quality. In electromigration experiments on YBCO thin film microbridges it was observed[6] that there was a threshold in the migration current density beyond which the effects turn from beneficial to deterious. Our annealing experiments seem to suggest that there is an analogous threshold, in temperature, between 400 °C and 450 °C.

Forth, the in-situ deposited STO overlayer appears essential. Its effectiveness in preventing oxygen loss from YBCO may be attributed to its high degree of crystallinity and epitaxy, a consequence of *in-situ* high temperature deposition.

Fifth, MgO was chosen for its excellent electrical insulation property. Such MgO has been used in our study of YBCO/noble metal interface resistivity study to provide isolation between the YBCO and the noble metal overlayer, and proved to be sufficient and reliable. For example, isolation test structures formed by sandwiching 75 nm of MgO between two metal cross strips with 0.1×0.1 mm^2 overlap area showed practically infinite resistance. Moreover, their integrity was not affected by annealing in argon gas flow for temperatures up to about 450°C. These qualities make MgO a good choice. In spite of its effectiveness in providing electrical isolation, our MgO layers appear to be less effective in proventing atomic diffusion of oxygen. Since they are deposited at room temperature, they are amorpuous and may well be porous, and may possibly have randomly located pinholes over the entire chip area (about 10×10 mm^2). Therefore there exist passageways for oxygen out-diffusion, which is accelerated by the elevated temperature during annealing. A modified method, i.e., the two-step sequential deposition of MgO appeared to work in the way that was anticipated, i.e., to misalign and hence seal off the pinholes formed in each of the two steps. However a firm conclusion can not be drawn based on just this one example.

ACKNOWLEDGEMENTS

This work was performed under the auspices of the U.S. Department of Energy. The YBCO films with $SrTiO_3$ overlayer used in annealing study were provided by the HTS group at TRW.

REFERENCES

1. J. BROWNE, "HTS Suppliers Take Aim At Commercial Markets," Microwaves & RF, 33, February, 1996.
2. W. A. PHILLIPS, "HTS Subsystem Analysis," Journal of Superconductivity, 8, 735 (1995).
3. T. VAN DUZER, "Superconductor-semiconductor hybrid devices, circuits and systems," Cryogenics, 28, 527 (1988).
4. Simon S. Cohen and Gennady Sh. Gildenblat, "Metal-Semiconductor Contacts and Devices, VLSI Electronics Microstructure Science, Volume 13," Academic Press, 1986.
5. S. J. Rothman, J. R. Routbort, and J. E. Baker, "Tracer diffusion of oxygen in $YBa_2Cu_3O_{7-\delta}$, " Phys. Rev. B 40, 8852 (1989).
6. B. H. Moeckly, D. K. Lathrop, and R. A. Buhrman, Phys. Rev. B 47, 400 (1993).

CALCULATION AND MEASUREMENT OF THE CRITICAL STATE IN SUPERCONDUCTING TAPES

K. L. Telschow and L. S. Koo

Idaho National Engineering Laboratory
Idaho Falls, ID 83415-2209

ABSTRACT

An integral equation approach to solving for the flux front profile in the critical state model is described. Both nonuniform external fields and demagnetizing geometries can be accommodated as long as cylindrical symmetry is preserved. Results for a sphere in a uniform external field and a tape in the field of an external coil parallel to the tape surface are presented.

INTRODUCTION

Quantitative determination of the local low field critical current density, $J_c(H=0)$, in a noncontacting manner is necessary for spatial uniformity inspection during fabrication of high T_c superconducting tapes. This can be accomplished by measuring the magnetic response of the sample with small source/pickup probe coils that spatially scan over the tape surface [1-3] and then using the Bean critical state model [4] to determine J_c from the measured magnetic hysteresis. In this model, the induced currents in the sample are either at the critical value or zero, forming a critical state region bounded by a "flux front profile". The response is calculated by summing the fields produced by the currents within this flux front. J_c can be inferred from the local magnetization measurements. However, demagnetization effects of the tape/coil geometry are not readily accounted for within the normal extension of the Bean critical state

model. This paper describes a method for predicting the flux front profile as a function of the external field that takes into account the demagnetizing effects of the sample surfaces. An integral equation technique is presented that is applicable to sample/probe geometries exhibiting cylindrical symmetry. The net magnetization signal detected by pickup coils is calculated and compared with experimental measurements.

THEORETICAL APPROACH

Whenever a superconducting material is placed in an applied magnetic field, a region of shielding current is induced. According to the Bean critical state model, the induced current begins at the material boundary next to the applied magnetic field and extends inward, satisfying $\nabla x\vec{B} = \mu_0\vec{J}_c$, where $\vec{B}$ is the magnetic induction vector and μ_0 is the free-space permeability. This leads to the net magnetic flux density in the material decreasing to zero at the flux front boundary. The region inside this boundary is free of magnetic field, shielded completely by the induced screening currents. This flux front surface inside a superconducting material can be defined as the surface on which the total magnetic field is zero; a vector equation defines the boundary [5]. However, as is proven in [6], the flux front can also be defined as a surface of zero vector potential, $\vec{A}$, where $\nabla x\vec{A} = \vec{B}$. The use of the vector potential simplifies the calculations since only one component is needed for problems of cylindrical symmetry. For problems with this symmetry, the induced currents inside the material can be modeled as coaxial loops, each carrying a current of constant value, J_c. Hence, the vector potential due to all of the induced currents is a volumetric integral sum of the single loops. The vector potential of a single current loop is well known. The unknown quantities in this integral are the flux front boundary, Ψ, which forms part of the integration limit, and the current density, J_c. In addition, the flux front boundary, Ψ, is a function of both space and the applied magnetic field. To simplify the calculations, the external applied field is normalized by J_c and a characteristic length. With this normalizing scheme, the total vector potential, A_{tot}, becomes a dimensionless implicit function of $\Psi(R,\beta)$, a normalized spatial variable, R, and the normalized applied field, β. Then the total vector potential is given by $A_{tot} = A_\beta - A_{J_c}$, where A_β and A_{J_c} are the vector potentials due to the external field, β, and the induced critical currents, J_c. The minus sign results from the shielding effect. For a given β, the position of the flux front surface is determined by finding spatial points where the total vector potential is zero. This is a difficult problem in general, but can be simplified by reduction to a single integral equation as follows. In general, β is a function of time. This technique deals only with the quasi-stationary states of the critical state. The time scale for changes in the external field is typically very much longer than that exhibited by flux line motion, so the model always assumes a sequence of stationary states uniquely defined by the history and present value of the external field. Changes in the external field then produce a corresponding change in the flux line profile position, but at all times the total vector potential

on this profile is zero. Therefore, a requirement for determining the flux penetration profile is that

$$\frac{\partial A_{tot}(\Psi(R,\beta),R)}{\partial \beta} = F\left(\Psi(R,\beta), \frac{\partial \Psi(R,\beta)}{\partial \beta}\right) = 0. \tag{1}$$

Equation (1) is often a nonlinear integral equation. As suggested by the critical state model, when the external field, β, is initially turned on, flux enters the superconducting material from the surface. Thus the initial profile, $\Psi(R, \beta=0)$, is the material surface. Substitution of the known surface profile into (1) yields a linear integral equation of the first kind for the unknown derivative of Ψ. The algorithm analyzed by Gold [7] is used to resolve (1). As the external field is increased to $\beta = \Delta\beta$, the new flux front profile is approximated by

$$\Psi(R,\beta = \Delta\beta) = \Psi(R,\beta = 0) + \frac{\partial \Psi(R,\beta = 0)}{\partial \beta} \cdot \Delta\beta. \tag{2}$$

This approximation is acceptable as long as the increment $\Delta\beta$ is sufficiently small. With this approximation the flux front profile at $\beta = \Delta\beta$ is known but its derivative is yet to be determined. This is the same situation as at the beginning when $\beta = 0$. The above procedure is repeated and the new β value determined. This methodology results in a progressive incremental numerical scheme in β and an iterative procedure for resolving (1) for each β. Once the flux front profile's dependence on the external field for the zero-field cooled (ZFC) case is known, then the response of the sample to a complete cycle of changes in the external field can be readily calculated, knowing $M_{ZFC}(\beta)$, as follows:

$$M_{\pm}(\beta) = \pm M_{ZFC}(\beta_{max}) \mp 2M_{ZFC}\left(\frac{\beta_{max} \mp \beta}{2}\right) \tag{3}$$

where (+) means decreasing $\beta_{max} > \beta > -\beta_{max}$ and (-) means increasing $-\beta_{max} \rightarrow \beta \rightarrow +\beta_{max}$ in the external field. Examples of this calculation for a spherical sample in a uniform external field and an infinite plate in the field of an external single loop source coil are described below.

SPHERE IN A UNIFORM EXTERNAL FIELD

In this example of a cylindrically symmetric application, let the radius of the sphere be r_0 and the flux front surface be described by $\rho(z,\beta)$ where the external field dependence is included in the normalization parameter $\beta = H_z^{ext}/(r_0 J_c)$. The configuration is depicted in Fig. 1. Also shown in

this figure are two flux fronts trapped inside the sphere as a result of extending the external field to a maximum value below the full penetration value. The total normalized vector potential at (r,z) is given below [6], where all lengths are normalized to the sphere radius $R = r/r_0$; $Z = z/r_0$; $\Psi = \rho/r_0$; etc.; and $\mu_0 a_\phi(R,Z;R',Z')$ is the vector potential at (R,Z) due to a single current loop at (R′,Z′)

$$A_\phi(R,Z,\beta) = \frac{\beta R}{2} - \int_{-1}^{1} dZ' \int_{\Psi(Z',\beta)}^{\sqrt{1-Z'^2}} dR'\, a_\phi(R,Z;R',Z') \tag{4}$$

A single integral equation describing the flux front surface for a sphere results

$$\int_{-1}^{1} dZ'\, a_\phi(\Psi(Z,\beta),Z;\Psi(Z',\beta),Z') \frac{-\partial\Psi(Z',\beta)}{\partial\beta} = \frac{\Psi(Z,\beta)}{2}. \tag{5}$$

The initial profile of the flux front is $\Psi(Z, \beta=0) = \sqrt{1-Z^2}$. All flux fronts for the ZFC case are obtained by following the aforementioned incremental iteration procedure. The full field penetration value obtained yields a normalized external field $\beta^*=0.789$. A value of $\pi/4$ is found analytically for a completely filled sphere. The numerical and analytical values agree to within 0.5% [6] which is consistent with the expected accuracy of the calculation procedure used. The subsequent magnetization hysteresis curve, $M(\beta)$, for the sphere due to a complete cycle of change in the external field can be obtained through equation (3). The results are given in Fig. 2, normalized by the full penetration magnetization $M^* = 3\pi r_0 J_c/32$.

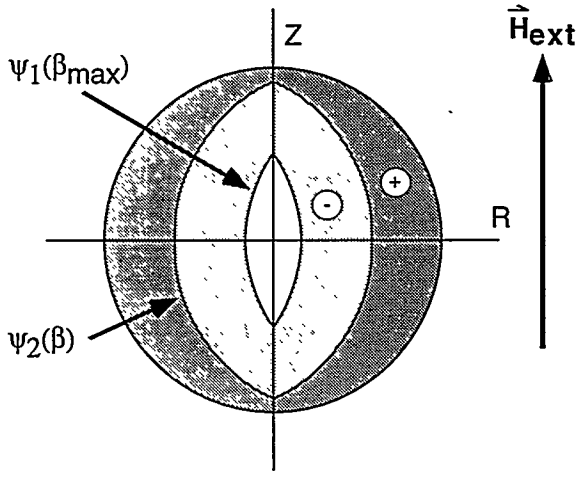

Fig. 1. Flux front profiles for a sphere.

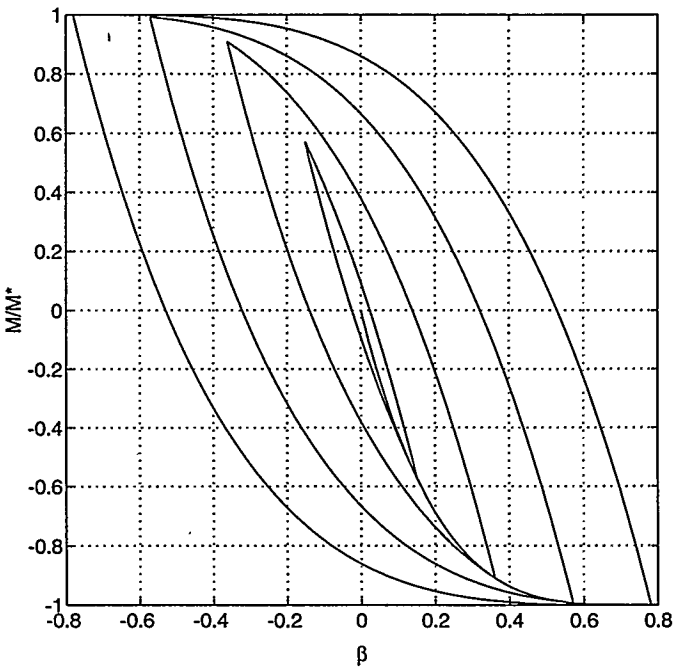

Fig. 2. Magnetization hysteresis of the sphere for various limiting fields.

TAPE GEOMETRY

A single circular coil above a superconducting infinite plate of thickness D is shown in Fig. 3. All geometrical lengths are normalized by the coil radius, r_c. The driving coil is placed at $(1,Z_c)$. The normalized external field is $\beta = I/J_c r_c^2$, where I is the current in the driving coil. The flux front profiles for the ZFC case are also shown in Fig. 3. At $\beta = 0$, $\Psi = 0$ coincides with the plate top surface. As β is increased to the next value, Ψ shows a profile that penetrates deepest directly under the driving coil. This deepest value of Ψ reaches the plate bottom edge at $\beta^* = 0.365$, for $D = -0.2$. Beyond this value, the flux front is broken up into two sections: an inner section, Ψ_1, which approaches R=0, and an outer section, Ψ_2, which approaches R=∞ as β increases. The intersections between Ψ_1, Ψ_2 and the bottom surface, $Z = D$, are denoted as R_1 and R_2, respectively. Before the bifurcation of the flux front surface, the total vector potential amplitude (normalized by $\mu_0 J_c r_c^2$) is

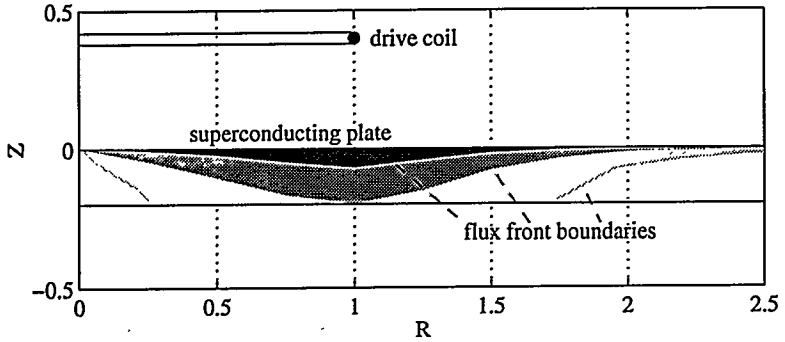

Fig. 3. Geometry for flux penetration in a plate for ZFC case with $\beta = 0.1$, 0.365 and 0.865.

$$A_{tot}(R,Z) = \beta a_\phi(R,Z;1,Z_c) - \int_0^\infty dR' \int_{\Psi(R',\beta)}^0 dZ'\, a_\phi(R,Z;R',Z') \tag{6}$$

where $\mu_0 a_\phi(R,Z;R',Z')$ is the vector potential at (R,Z) due to a unit current loop at (R′,Z′). A single integral equation results for the flux front surface

$$\int_0^\infty dR'\, a_\phi(R,\Psi(R,\beta);R',\Psi(R',\beta)) \frac{-\partial\Psi(R',\beta)}{\partial\beta} = a_\phi(R,\Psi(R,\beta);1,Z_c). \tag{7}$$

The initial profile of the flux front is $\Psi(R,\beta=0) = 0$. As β is increased beyond β^*, the flux front surface Ψ will become two separate surfaces, Ψ_1 and Ψ_2. The total vector potential becomes

$$\begin{aligned} A_{tot}(R,Z) = {} & \beta a_\phi(R,Z;1,Z_c) - \int_0^{R_1(\beta)} dR' \int_{\Psi_1(R',\beta)}^0 dZ'\, a_\phi(R,Z;R',Z') \\ & - \int_{R_1(\beta)}^{R_2(\beta)} dR' \int_D^0 dZ'\, a_\phi(R,Z;R',Z') - \int_{R_2(\beta)}^\infty dR' \int_{\Psi_2(R',\beta)}^0 dZ'\, a_\phi(R,Z;R',Z') \end{aligned} \tag{8}$$

With Ψ_1' and Ψ_2' denoted as $\Psi_1(R',\beta)$ and $\Psi_2(R',\beta)$, two coupled equations result [8]

$$\int_0^{R_1(\beta)} dR'\, a_\phi(R,\Psi_1;R',\Psi_1')\cdot\frac{-\partial\Psi_1'}{\partial\beta}+\int_{R_2(\beta)}^{\infty} dR'\, a_\phi(R,\Psi_1;R',\Psi_2')\cdot\frac{-\partial\Psi_2'}{\partial\beta}=a_\phi(R,\Psi_1;1,Z_c) \quad (9a)$$

and

$$\int_0^{R_1(\beta)} dR'\, a_\phi(R,\Psi_2;R',\Psi_1')\cdot\frac{-\partial\Psi_1'}{\partial\beta}+\int_{R_2(\beta)}^{\infty} dR'\, a_\phi(R,\Psi_2;R',\Psi_2')\cdot\frac{-\partial\Psi_2'}{\partial\beta}=a_\phi(R,\Psi_2;1,Z_c). \quad (9b)$$

These two equations couple both flux fronts together. In the first equation, the observation points are on Ψ_1, while in the second equation the observation points are on Ψ_2. These two equations, expressed in matrix format, are

$$\begin{bmatrix} K_{11} & K_{12} \\ K_{21} & K_{22} \end{bmatrix}\begin{pmatrix} f_1 \\ f_2 \end{pmatrix}=\begin{pmatrix} a_1 \\ a_2 \end{pmatrix} \quad \text{where} \quad K_{12}f_2=\int_{R_2(\beta)}^{\infty} dR'\, a_\phi(R,\Psi_1;R',\Psi_2')\cdot\frac{-\partial\Psi_2'}{\partial\beta}, \text{ etc.} \quad (10)$$

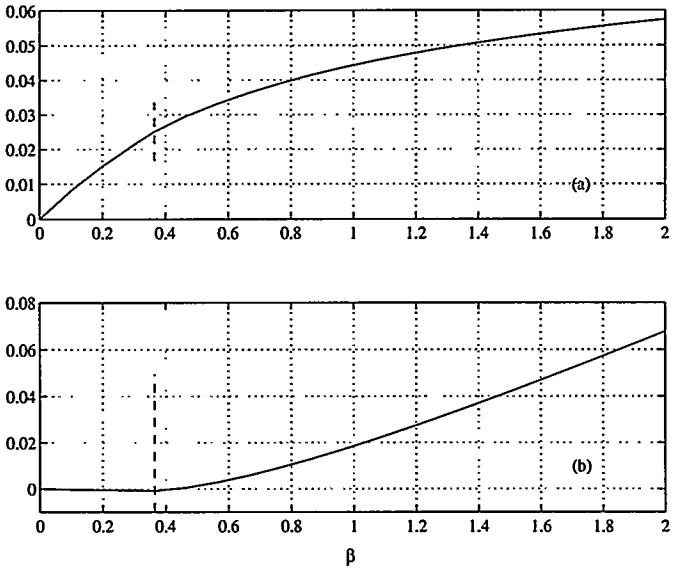

Fig. 4. A_{J_c} for a coil above the plate (a) and A_{tot} for a coil beneath the plate (b).

The incremental and iterative procedures were employed to resolve the two separate flux fronts simultaneously. Two simulated measurement examples are given in Figs. 4a and 4b. In these examples, $r_c = 0.5$ mm, $Z_c = 0.4$, and $D = -0.2$. In Fig. 4a, the normalized screening current vector potential amplitude, A_{J_c}, at the driving coil position (1,0.4) is given, simulating the measurement results found above the sample with a top balanced coil. In Fig. 4b, the normalized total vector potential amplitude, A_{tot}, is given at (1,-0.6), simulating the measurement results found beneath the sample with a single unbalanced coil. The vertical dashed line signifies the value β^* where the flux front fully penetrates to the plate bottom surface.

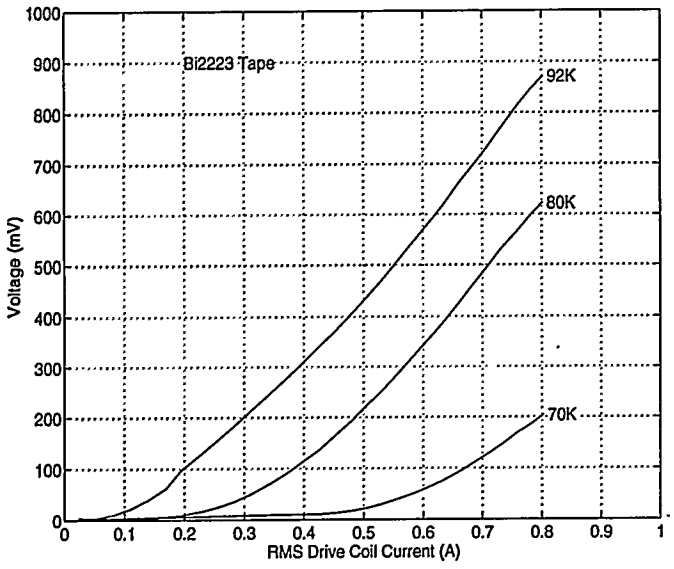

Fig. 5. Measured bottom coil signal amplitudes for different temperatures.

The experimental geometry was that of a single layer superconductor plate deposited between two outside silver layers. Tape samples of Pb-BiSrCaCuO (2223 phase) produced by the powder-in-tube method [3,9] were measured with a small probe source coil (13 turns of #36 copper wire, 1 mm inside diameter). Balanced opposing pickup coils (5 turns each of #36) were wound over the source coil, producing a small source/pickup probe that could be scanned over the sample surface in a liquid nitrogen bath. An additional pickup coil (5 turns #36 copper wire, 1 mm diameter) was positioned below the tape sample. Lift-off distances for both top and bottom coils were about 0.7 mm. Fig. 5 shows the measured results from the bottom coil at one position on the tape for three different temperatures. These results, which are qualitatively similar to the theoretical results of Fig. 4b, represent the magnetization due only to the induced screening currents within the flux front. The shielding effect is clearly visible and, by extrapolation, a unique point corresponding to full plate penetration can be estimated. The local critical current density can then be determined from the corresponding value of β.

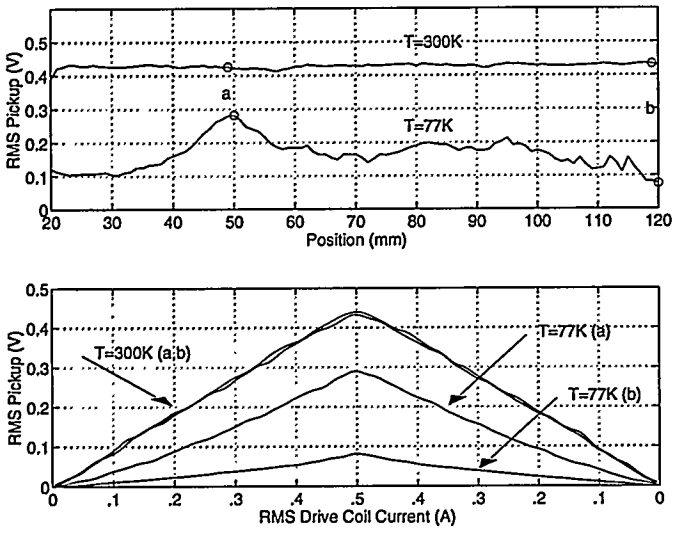

Fig. 6. Maximum signal along a tape (top) and corresponding RMS signal amplitudes (bottom) as a function of the source coil current.

Tapes produced by the "powder in tube" method exhibit thickness variations as well as inhomogeneity in the superconducting layer. Nevertheless, the above approach can be used to provide a measure of uniformity and local critical current density. Fig. 6 shows typical results for a scan of another small probe along a tape, produced by the powder in tube method [9]. Significant variations are observed due to local microstructural inhomogeneities. Detailed information like that shown in Fig. 6 is helpful in

locating problems associated with intergrain connections and thickness or porosity defects.

CONCLUSION

A method has been outlined for calculating the flux front profile for a superconducting sample in either a uniform or nonuniform applied magnetic field possessing cylindrical symmetry. This technique extends the Bean critical state model by fully accounting for demagnetizing effects. The method relies upon finding the flux front penetration profile, which is done by resolving a linear integral equation of the first kind. Measurement-induced voltages and the entire hysteresis loop response can be found by extension of the ZFC magnetization response with a changing external field. Other measured quantities relating to the critical state can be calculated directly from the hysteresis loop if the time dependence of the external field is known.

ACKNOWLEDGMENT

The authors thank M. T. Lanagan of Argonne National laboratory for the tape samples used and K. K. Haulenbeek and F. Bruneel for help in obtaining the measurement results. This work was supported by the U.S. Department of Energy, Office of Basic Energy Sciences, under DOE Idaho Operations Office Contract DE-AC07-94ID13223.

REFERENCES

1. A. M. Campbell and J. E. Evetts, *Critical Currents in Superconductors*, Taylor & Francis Ltd., London, (1972).
2. K. L. Telschow and T. K. O'Brien, *Appl. Phys. Lett.* 59, 730 (1991).
3. K. L. Telschow, T. K. O'Brien, M. T. Lanagan and D. Y. Kaufman, *IEEE Trans. Magn.* 3 (1), part III, 1643 (1993).
4. C. P. Bean, *Phys. Rev. Lett.* 8, 250 (1962) and *Rev. Mod. Phys.* 36, 31 (1964).
5. R. Navarro and L. J. Campbell, *Phys. Rev. B* 44, 10146 (1991).
6. K. L. Telschow and L. S. Koo, *Phys. Rev. B* 50 (10), 6923 (1994).
7. R. Gold, Report ANL-6984, Argonne National Laboratory, December (1964).
8. L. S. Koo and K. L. Telschow, *Phys. Rev. B* 53, 8743 (1996).
9. Samples were provided by M. T. Lanagan at Argonne National Laboratory.

SURFACE AND DEFECT MORPHOLOGIES IN ANISOTROPIC ELASTIC AND PIEZOELECTRIC SOLIDS

Huajian Gao* and David M. Barnett**
Division of Applied Mechanics* and Department of Materials Science & Engineering**
Stanford University
Stanford, CA 94305

ABSTRACT

We investigate issues related to the equilibrium and stability of surface and line defect morphologies in both piezoelectric and anisotropic elastic solids. Following our previous efforts which established that mechanical stresses in purely elastic solids can promote instability of an initially flat surface with respect to surface roughening, we show that the (initially flat) interface between two dissimilar piezoelectric solids can be unstable when subjected to coupled electromechanical loading. Quite recent cross-sectional observations of electrodeposited thin films by Japanese and British researchers provide experimental confirmation of these predictions. We also investigate the occurrence of equilibrium arrangements (zero Peach-Koehler force arrangements) of line defects (dislocations) in anisotropic elastic crystals in the absence of externally applied stresses. Contrary to prevailing opinion, equilibrium arrangements of dislocations under no externally applied stresses appear to be the rule rather than the exception. The existence of such "zero stress arrangements" is fundamental to developing micromechanical models of plastically deforming solids.

INTRODUCTION

In the present work we focus our attention on (i) surface instabilities induced by electromechanical loading in piezoelectric bi-crystals and upon (ii) equilibrium arrangements of line defects (dislocations) in crystals in the absence of externally applied stresses. The former problem (i) represents an extension of our previous study of a purely elastic solid [1] and of a piezoelectric half-space [2], which has established that mechanical stress can induce surface roughening of an initially flat surface, while electrical loading may act to either stabilize or destabilize a flat surface. These results may be of extreme importance for the understanding of crack formation in defect free materials as well for uncovering possible mechanisms for misfit dislocation generation in thin films

deposited on substrates. The present extension allows one to address the broad issue of controlling flat surface/interface instability in materials which may be isotropic or anisotropic, purely dielectric or purely elastic, or piezoelectric, which, quite obviously, has important implications for the fabrication of dielectric and piezoelectric thin films. The motivation for investigating the latter problem (ii) is perhaps best summarized in a very short presentation by Head, et al [3], who noted that although there is total agreement about the role of dislocations in explaining strain hardening in metals, such a vast range of dislocation behavior and arrangements has been observed experimentally that there is little agreement as to which observations are the more important. It seems as if the issue may have to be decided on theoretical grounds by mathematical modeling of dislocation plasticity, and we begin by examining the simplest of such problems, namely, the determination of self-equilibrated dislocation arrangements in solids which are in the unloaded state (zero externally applied stress) following inhomogeneous plastic straining.

SURFACE INSTABILITIES INDUCED BY ELECTROMECHANICAL LOADING

Stress-induced surface instabilities in purely elastic media have been discussed by Gao [1] in connection with diffusive crack formation and with misfit dislocation generation in strained heteroepitaxial thin films. The instability (roughening) of an initially flat surface is driven by the release of stored strain energy due to flaw formation and is opposed by the formation of new surface and the associated increase in surface energy of the system (Asaro and Tiller [4]). Chien and Gao [2] have studied the surface roughening of a piezoelectric half-space when the half-space boundary is either insulating or conducting and have shown that it is indeed possible for electrical loading to help stabilize the initial surface against roughening. The present work treats two dissimilar piezocrystals (half-spaces) joined by perfect electroelastic bonding and studies the stability of the initially flat interface between the two crystals with respect to small interfacial undulations. An analysis of this problem represents an important extension in two respects, namely, (i) it allows us to study roughening of an internal interface as opposed to an external surface, and (ii) depending on the choice of physical properties chosen for the two crystals, either crystal may be considered as isotropic or anisotropic, purely dielectric or purely elastic, or piezoelectric. The former, (i), is important because internal interfaces afford sites for defect initiation in real configurations of technological importance, while the latter, (ii), allows us to study bi-material configurations of importance in modern capacitor, transducer, or integrated circuit fabrication. The ability to control interfacial stability through appropriately coupled electromechanical loading is of paramount significance in these technologies.

Editorial space limitations preclude a complete presentation of the instability analysis, but we shall endeavor to present a brief description of our procedure. The complete treatment is given in Chien, et al [5]. The constitutive relations for a linear piezoelectric medium are [6,7]

$$T_{ij} = C_{ijkl}S_{kl} - e_{kij}E_k \tag{1}$$

$$D_i = e_{ikl}S_{kl} + \varepsilon_{ij}E_j \tag{2}$$

where C_{ijkl} are the stiffnesses measured at constant strain, e_{ijk} the piezoelectric stress constants, and ε_{ij} the permittivities measured at constant strain. T_{ij} , S_{kl}, E_k, and D_i represent components of stress, strain, electric field, and electrical induction, respectively, with

$$S_{kl} = \frac{1}{2}\left(u_{k,l} + u_{l,k}\right) \text{ and } E_k = -\phi_{,k} \tag{3}$$

where $\mathbf{u}$ and ϕ represent displacement and electric potential, respectively. With no body forces or free charges, the governing equations of linear piezoelectricity (quasistatic approximation) are

$$T_{ij,i} = 0 \text{ and } D_{i,i} = 0. \tag{4}$$

The present work considers the stability of an initially flat piezoelectric interface between two semi-infinite dissimilar piezoelectric materials, I (the upper medium) and II (the lower medium), subjected to arbitrary electromechanical loading conditions (Figure 1). In particular we consider electromechanical states which are plane in the sense that all fields are independent of x_3.

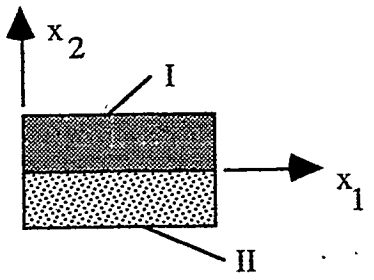

Figure 1. An Initially Flat Interface Between Two Piezoelectric Solids

The composite piezoelectric problem may be solved using the Stroh formalism [8], originally developed for anisotropic elasticity, as extended to the piezoelectric case by Lothe and Barnett [7,9,10]. The important feature to note is that the piezoelectric problem for the two bonded crystals is solved subject to the interfacial boundary conditions that mechanical displacement, normal component of electrical induction, mechanical tractions, and electrostatic potential must be continuous across the interface $x_2 = 0$. To examine stability of the flat interface with respect to small perturbations, we imagine treating the same problem when the interface is now described by a cosinusoidal form, say

$$x_2 = A(x_1) = A\cos kx_1. \quad k = 2\pi/\lambda. \tag{5}$$

The solution for the perturbed interface may be written in terms of two four-vector potentials $\psi^{(i)}$, i = I, II, associated with the respective media, namely,

$$\psi^{(i)} = \psi^{(i0)} + \Lambda^{(i)} \tag{6}$$

where $\Lambda^{(i)}$ represents the effect of the perturbation. Interfacial continuity conditions require that

$$\left[\left|\mathrm{Re}\,\psi^0\right|\right] = 0 \text{ and } \left[\left|\mathrm{Im}\left(\mathbf{Y}\psi^0\right)\right|\right] = 0 \tag{7}$$

where $\mathbf{Y}^{(i)}$ is the 4 x 4 hermitian Stroh admittance matrix for the half-space (i) and $\left[\left|\ \right|\right]$ means the "jump" across the interface $x_2 = 0$. Applying first order perturbation theory allows us to deduce that the perturbed potentials satisfy

$$\left[\left|\mathrm{Re}\,\Lambda\right|\right] = -A\left[\left|\mathrm{Re}\left(\psi^0_{,2}\right)\right|\right] \text{ and } \left[\left|\mathrm{Im}(\mathbf{Y}\Lambda)\right|\right] = -A\left[\left|\mathrm{Im}\,\mathbf{Y}\psi^0_{,2}\right|\right]. \tag{8}$$

Using (8) it is easy to solve for the perturbed potentials in terms of the unperturbed potentials and to compute the change in electrical enthalpy (over one wavelength) induced by the perturbation. Integration of the electrical enthalpy density

$$w = \frac{1}{2}\left(T_{ij}S_{ij} - D_iE_i\right) \tag{9}$$

over the infinite slab between $x_1 = 0$ and $x_1 = \lambda$ shows that the enthalpy change ΔW_λ due to the perturbation is a quadratic form in the two 4-vectors

$$\mathbf{t}^0 = -\mathrm{Re}\left[\left|\psi^0_{,2}\right|\right] \text{ and } \mathbf{e}^0 = \mathrm{Im}\left[\left|\mathbf{Y}\psi^0_{,2}\right|\right], \text{ namely} \tag{10}$$

$$\Delta W_\lambda = \frac{\pi}{2}A^2\left\{\left(\mathbf{t}^0 \bullet \mathbf{a} \bullet \mathbf{t}^0\right) + \left(\mathbf{e}^0 \bullet \mathbf{b} \circ \mathbf{e}^0\right) + 2\left(\mathbf{t}^0 \bullet \mathbf{c} \bullet \mathbf{e}^0\right)\right\} \tag{11}$$

where the 4 x 4 matrices **a**, **b**, and **c** depend on $\mathbf{Y}^{\mathrm{I}}$ and $\mathbf{Y}^{\mathrm{II}}$. One notes that ΔW_λ is independent of λ. The total energy change over one wavelength is the sum of the electrical enthalpy and the surface energy change [5] and is given by

$$\Delta E_{tot} = \Delta W_\lambda + \frac{\gamma A^2 \pi^2}{\lambda}, \tag{12}$$

where γ is the specific interfacial energy. The question of stability of the initially flat interface is studied by examining the sign of the total energy change, i.e., does the undulation raise or lower the energy of the system? If $\Delta E_{tot} > 0$, the interface is stable against perturbation, while if the total energy is negative for at least one perturbation wavelength, a wavy interface is preferred energetically. Clearly, at short wavelengths the surface energy contribution dominates, while the enthalpy should dominate at long wavelengths.

When the electrical enthalpy change tends to destabilize a flat surface (when $\Delta W_\lambda < 0$), a critical wavelength λ_{cr} exists such that

$$\Delta E_{tot}(\lambda) \geq 0 \text{ when } \lambda \leq \lambda_{cr}. \tag{13}$$

Quite apart from being a criterion for stability, the critical wavelength has important implications for the kinetics of any destabilizing mechanism. If diffusion is a possible mechanism for interface roughening, the larger the critical wavelength, the farther matter must diffuse, and thus longer times are required for destabilization. For large critical wavelengths, the interface may be considered stable for all practical purposes. In [5] we have examined a variety of electromechanical loading conditions and material possibilities for media I and II, e.g., vacuum/piezocrystal, dielectric fluid/piezoelectric solid, etc. In particular in [5] it is shown that for a (thin) insulating film deposited on a capacitor plate under constant imposed voltage (a configuration seen in the fabrication of thin film capacitors by anodic oxidation [11]), both mechanical and electrical loading tend to destabilize an interface; for other configurations it is shown that tangential discontinuities in **D** can promote interface stability in the presence of mechanical loading.

Almost simultaneously with the appearance of our paper [5] in the March, 1996 issue of **Proceedings of the Royal Society**, a paper by Shimizu, et al [12], entitled "The scope for studies of thin surface films on metals and alloys by transmission electron microscopy of ultramicrotomed sections" appeared in **Philosophical Transactions of the Royal Society of London.** As the title indicates, these authors used high resolution analytical electron microscopy to examine microtomed sections of films deposited on substrates. They observed that inert markers originally delineating a flat surface in barrier oxide films later delineated a roughened interface following new oxide growth. In addition, their electron micrographs show unmistakable evidence of undulating interfaces between barrier oxide films formed on low voltage type capacitor foil anodized under industrial conditions. Interfaces in electrodeposited Ni-P alloys show undulations, compositional differences, and different layers of differing crystallinity. We believe these experimental results provide striking and convincing evidence for the validity of the theoretical predictions we have presented in [5].

SELF-EQUILIBRATED DISLOCATION ARRAYS

If a solid is subjected to inhomogeneous plastic deformation followed by complete unloading, it is well known that the medium will be in a state of residual stress. On a microscopic scale there is ample experimental evidence that, in the unloaded state, the solid is filled with stationary dislocations, and that the residual stress state is the stress field due to the locked-in dislocation configuration, with the dislocation density typically varying between 10^5 to 10^8 dislocations per square centimeter. These locked-in dislocation distributions are, presumably, in equilibrium in the sense that they arrange themselves so as to minimize the potential energy of the unloaded solid. Alternatively, we may regard the Peach-Koehler force on each dislocation (the negative of the variation of the total energy of the solid with respect to an infinitesimal virtual displacement of each dislocation) as vanishing. The question arises as to whether it is truly possible to have self-equilibrated dislocation configurations in a crystal in the absence of applied stresses. This issue is more than academic, since most direct observations of dislocations in crystals are made on unloaded thin film specimens using transmission electron microscopy. An interpretation of such observations depends on an understanding of either the possibility of the existence of self-equilibrated dislocation configurations or the constraints (for example, rendering some dislocations immobile by "pinning") necessary to ensure their existence. As pointed out by Head, et al [3], there exist trivial examples of such self-equilibrated arrays, namely those distributions which produce only crystal rotations, but no elastic strains; these redundant distributions (called "impotent distributions" by Mura [13]) have no residual stress fields associated with them.

Tighe [14] has studied analytically issues associated with self-equilibrated arrays, but until Lubarda, et al, [15] numerically studied self-equilibrated arrays in elastically isotropic solids, no one had dealt with the issue of self-equilibrated arrays of large numbers of dislocations. Lubarda, et al, indeed showed that self-equilibrated dislocation structures can exist, sometimes with pinning constraints and sometimes without. Our present work has sought to extend the methodology in [15] by allowing for the inclusion of elastic anisotropy, and by adopting a more inclusive and efficient method for treating doubly periodic arrays so as to account for quite large numbers of dislocations. The latter extension is enabled by our ability to sum in closed form the interaction energy between a single dislocation and an infinite dislocation wall, which is significant in view of the long range nature of individual dislocation stress fields.

As the ability to determine equilibrated dislocation configurations involves minimizing the interaction energy between all pairs of dislocations, we have shown that in an infinite solid of arbitrary anisotropy the elastic interaction energy between two straight dislocations at (x_1, y_1) and (x_2, y_2), respectively, (Burgers vectors $\mathbf{b}_1$ and $\mathbf{b}_2$) is

$$E_{int} = \frac{1}{2\pi i}\sum_{\alpha=1}^{6} \pm L_{i\alpha} L_{s\alpha} b_{1i} b_{2s} \ln \frac{(x_1 - x_2) + p_\alpha (y_1 - y_2)}{R} \tag{14}$$

where p_α and $\mathbf{L}_\alpha$ are the anisotropic elastic Stroh [8] eigenvalues and Stroh auxiliary eigenvectors, respectively, and the $\pm$ sign is the sign of Im (p_α). R is an arbitrary constant with dimensions of length; it is of no importance as regards minimization of the total interaction energy. As with Lubarda, et al, we note that the most natural way of studying equilibrium arrays of large numbers of dislocations is to study doubly periodic arrangements of straight dislocations and to focus our attentions on a single repeating "cell". Figure 2 depicts nine such cells of a doubly periodic arrangement with three dislocations per cell, merely for purposes of illustration. In practice we compute with hundreds of dislocations per cell.

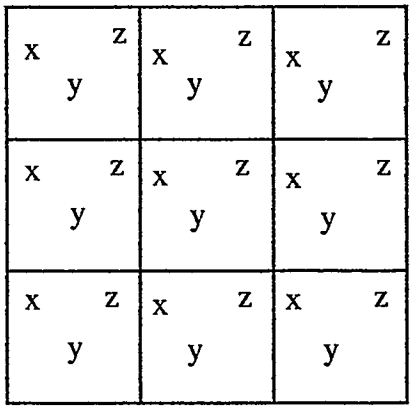

Figure 2. A portion of a doubly periodic arrangement of dislocations.

If we wish to compute the interaction energy for the doubly periodic arrangement shown in Figure 2, it suffices to focus our attention on one unit cell and to compute the interaction of the dislocation labeled "x" with the infinite vertical walls of "x", "y", and "z" dislocations throughout all space. However, and this point seems to have gone unnoticed, the interactions of dislocation x with its own wall or with all other "x" walls is independent of where dislocation "x" sits in the cell, i.e., the variation of this interaction with a virtual displacement of dislocation "x" vanishes; obviously a similar result holds for "y" and "z" dislocations. Thus we need only focus our attentions on the interaction between dislocation x in one cell with all parallel "y" and "z" walls, and on the interaction between dislocation y in the same cell with all parallel "x" and "z" walls, etc. (being careful to count the interactions only once). The second computational savings results from our ability to show that the interaction elastic energy between a single dislocation at (X,Y) in the cell under consideration with a vertical wall containing a dislocation at (X',Y') in the same cell can be expressed exactly as

$$E_{int} = \frac{1}{2\pi i} b_i^X b_s^{X'} \sum_{\alpha=1}^{6} \pm L_{i\alpha} L_{s\alpha} \ln\left[\sin \frac{\pi\left((X - X') + p_\alpha (Y - Y')\right)}{p_\alpha h}\right] \qquad (15)$$

where h is the periodic vertical spacing. The position-dependent part of the total interaction energy per cell is computed by summing terms such as (15) with X' replaced by X' + kH (k= $\pm 1, \pm 2, \ldots \pm \infty$; H is the horizontal periodicity). Although these infinite sums formally diverge, we have shown that the position-dependent part is well-defined and stems from a series whose terms decay exponentially as $|k| \rightarrow \infty$. Thus, we have available the ingredients for an energy minimization scheme which rigorously handles **all** wall dislocations in the vertical direction and whose decay with separation along the horizontal is sufficiently rapid that only a limited number of walls outside the cell under consideration need be considered for good convergence to be obtained.

The most significant results obtained using (15), which are presented with the lecture accompanying this work, involved filling a unit cell of a doubly periodic structure with between 100 and 400 dislocations, distributed on equally spaced parallel horizontal slip planes, with the number of dislocations on a given slip plane assigned by a random number generator, and with the sign (positive or negative) of the dislocations on any slip plane assigned at random. With an equal number of positive and negative dislocations, under zero applied stress an equilibrium distribution **was always found** using a conjugate gradient algorithm. The equilibrium distributions obtained are apparently different for different assigned starting configurations, which illustrates the non-uniqueness of the equilibria obtained. Once the equilibria were found, we examined the Peach-Koehler force on each dislocation in the repeating cell at equilibrium. For typical dislocation densities (which set the length scale for the problem) all Peach-Koehler forces were well below accepted values of lattice friction stresses, indicating that self-equilibrated dislocation distributions under no external stress are the rule rather than the exception. With a 50-50 mix of positive and negative dislocations, no constraints such as "pinning" selected dislocations are necessary to produce equilibrium. The non-uniqueness of these distributions is perhaps at the root of the non-uniqueness of experimental observations of locked-in dislocation configurations in the unloaded state. Like Lubarda, et al, we found that when the dislocation mix is far from a 50-50 mix of positive and negative edge dislocations, the equilibria obtained involve separation of the initial distribution into dislocation walls.

With significantly large numbers of dislocations present, it has yet to be shown that self-equilibrated dislocation distributions occupying only a **finite** portion of either a bounded or an unbounded solid can be found without constraining certain dislocations by pinning. It is possible that by dealing with partial dislocations separated by stacking faults such distributions could be found without invoking pinning constraints. Finally, examining these same issues within the context of the theory of continuously distributed dislocations is indeed worthy of attention, and will be pursued in the future.

ACKNOWLEDGMENTS

This work was performed under a grant to Stanford University from the United States Department of Energy.

REFERENCES

1. H. GAO, "Morphological Instabilities Along Surfaces of Anisotropic Solids," in *Modern Theory of Anisotropic Elasticity and Applications*, pp. 139 - 150, eds. J. J. Wu, T. C. T. Ting, and D. M. Barnett, SIAM, Philadelphia (1991).

2. N. CHIEN and H. GAO, "Stress-Induced Roughening Along Surfaces of Piezoelectric Materials," *Proceedings 11th Symposium on Energy Engineering Sciences*, pp. 16 - 23, Argonne National Laboratory (May, 1993).

3. A. K. HEAD, S. D. HOWISON, J. R. OCKENDON and S. P. TIGHE, "Mathematical Modeling of Dislocation Plasticity," *Physica Scripta*, **T44**, pp. 135 -136 (1992).

4. R. J. ASARO and W. A. TILLER, "Interface Morphology Development During Stress Corrosion Cracking: Part 1. Via Surface Diffusion," *Metallurgical Transactions*, **3**, pp. 1789 - 1796 (1972).

5. N. CHIEN, H. GAO, G. HERRMANN, and D. M. BARNETT, "Diffusive Instabilities Induced by Electromechanical Loading," *Proceedings of the Royal Society, London*, **A**, **452**, pp. 527 - 541 (1996).

6. H. F. TIERSTEN, *Linear Piezoelectric Plate Vibrations*, Plenum Press, N. Y. (1969)

7. D. M. BARNETT and J. LOTHE, "Dislocations and Line Charges in Piezoelectric Insulators," *Physica Status Solidi (b)*,**67**, pp. 105 - 111 (1975).

8. A. N. STROH, 'Steady State Problems in Anisotropic Elasticity," *Journal of Mathematics and Physics*, **41**, pp. 77 - 103 (1962).

9. J. LOTHE and D. M. BARNETT, "Integral Formalism for Surface Waves in Piezoelectric Crystals: Existence Conditions", *Journal of Applied Physics*, **47**, pp. 1799 - 1807 (1976).

10. J. LOTHE and D. M. BARNETT, "Further Development of the Theory for Surface Waves in Piezoelectric Crystals," *Physica Norvegica*, **8**, pp. 239 - 254 (1977).

11. L. I. MAISSEL and R. GLANG, *Handbook of Thin Film Technology*. McGraw - Hill, N. Y. (1970)

12. K. SHIMIZU, K. KOBAYASHI, G. E. THOMPSON, G. C. WOOD, and P. K. SKELDON, "The Scope for Studies of Thin Films on Metals and Alloys by Transmission Electron Microscopy of Ultramicrotomed Sections," *Philosophical Transactions of the Royal Society, London*, **A**, **354**, pp. 213 - 235 (1996).

13. T. MURA, *Micromechanics of Defects in Solids, 2nd Edition*, Martinus Nijhoff Publishers, Dordecht, Netherlands (1987).

14. S. P. TIGHE, "Continuum Modeling of Dislocations", *Thesis for transferal to D. Phil. status in Mathematics*, Michaelmas Term, Oxford University (1990).

15. V. A. LUBARDA, J. A. BLUME, and A. NEEDLEMAN, 'An Analysis of Equilibrium Dislocation Distributions," *Acta Metallurgica et Materialia*, **41**, pp. 625 - 642 (1993).

ELASTIC-PLASTIC FRACTURE MECHANICS OF STRENGTH-MISMATCHING

D. M. Parks, S. Ganti and F. A. McClintock

Massachusetts Institute of Technology
Cambridge, MA 02139, USA.

ABSTRACT

Approximate solutions to stress-fields are provided for a strength-mismatched interface crack in small-scale yielding (SSY) for non-hardening and low hardening materials. Variations of local deformation intensities, characterized by a $J-$type contour integral, are proposed. The softer material experiences a higher deformation intensity level, J_S, while the harder material sees a much lower deformation intensity level, J_H, compared to that obtained from the applied J near the respective homogeneous crack-tips. For a low hardening material, the stress fields are obtained by scaling from an elastic/perfectly-plastic problem, based on an effective mismatch, M_{eff}, which is a function of mismatch, M, and the hardening exponent, n. Triaxial stress build-up is discussed quantitatively in terms of M. The influence of strength-mismatch on cleavage fracture is discussed using Weibull statistics.

INTRODUCTION

Conventional fracture mechanics deals with predicting fracture in large structures by testing small specimens. It relies on the notion that a few parameters (eg: $K_I - T$, $J_I - Q$) characterize the crack-tip stress and deformation fields. Crack-initiation and growth are assumed to occur when these parameters reach critical values (which depend on the geometry and loading) (eg: K_{Ic}, J_{Ic}). In such cases, material resistance is characterized by these few parameters. While this technology, developed for homogeneous materials, is being used for welded joints based more on empiricism than on fundamentals, effective use of this technology is inhibited by the geometrical and material inhomogenities in a weld. The growing concern for quantifying structural resistance in welded structures can be seen from the formation of numerous European and Japanese groups (EPI, FCWRP etc.) to study weld-related fracture problems.

A schematic of a weld is shown in Fig. 1. Complications in the analysis of welded joints include the strength mismatch, location and orientation of the crack with respect to the fusion line, and geometry of the weld. The mismatch in strength between a weld metal and its base plate is termed under-matching and over-matching, respectively,

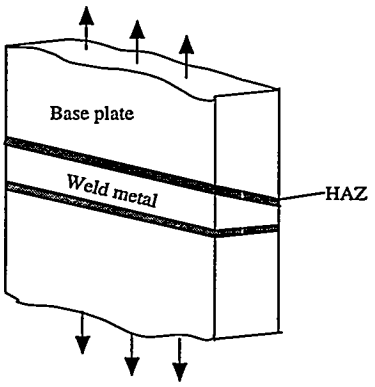

Figure 1: Schematic of a weld.

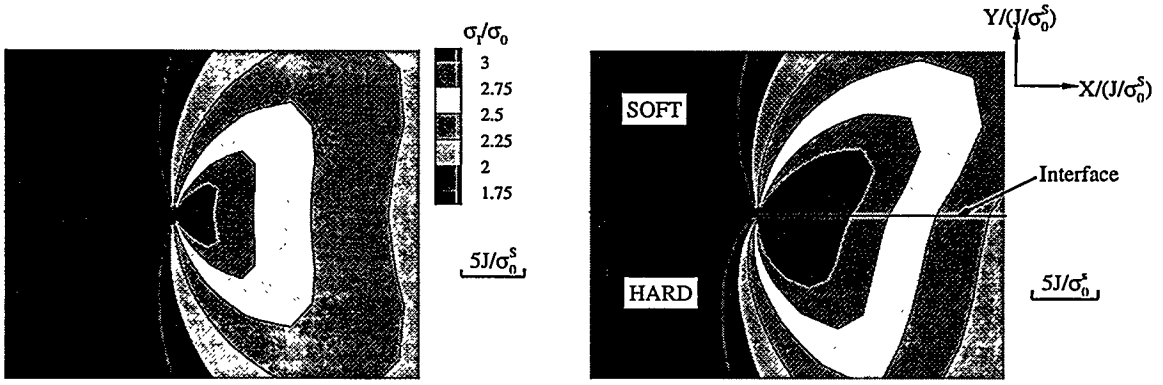

Figure 2: Contours of maximum principal stress for homogeneous and mismatched specimens. (a) Homogeneous (b) Mismatched, $M = 1.5$.

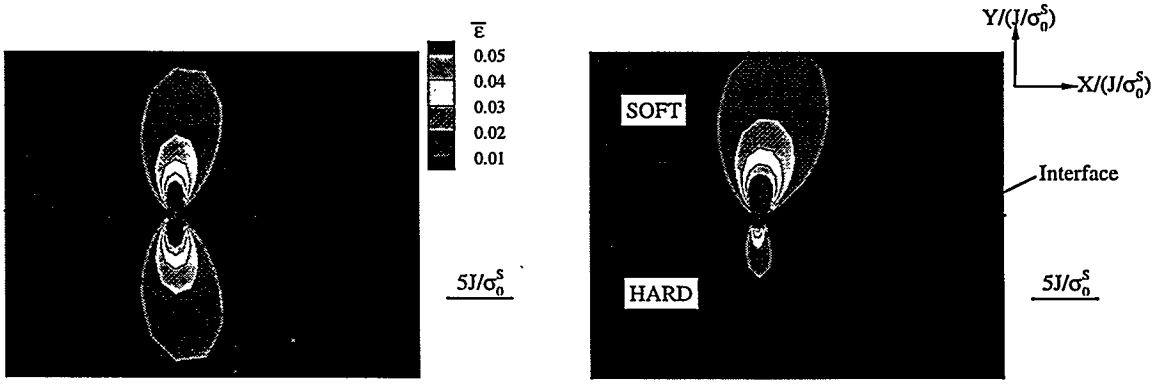

Figure 3: Contours of equivalent plastic strain for homogeneous and mismatched specimens. (a) Homogeneous (b) Mismatched, $M = 1.5$.

if the weld metal yield strength is lower or higher than the base material. Unwanted mis-matching can occur when either the strength of the base or the weld metals deviate from the minimum specified. The analysis is further complicated for a crack located near the fusion line due to the strength and microstructural gradients across the heat affected zone (HAZ).

The variation in properties across the weld influences the development of plastic deformation and stress, and hence the relationship between the resistance and applied loading. At a more fundamental level, it is not clear how measures like the J-integral and $CTOD$ characterize the crack-tip fields in mismatched specimens, even in small scale yielding (SSY). Studies by Koçak et al. [1] and Toyoda et al. [2, 3, 4] show that toughness of the Heat Affected Zone (HAZ) as characterized by $CTOD_c$ decreases with increasing weld metal strength. Due to asymmetric plastic zone development, the slope of J vs Δa decreased for an interface crack, compared to the corresponding base metal [1]. As stated by Koçak et al., the "apparent toughness" of the HAZ depends not only on the microstructure of hardened zones, but also on the mechanical properties of the adjacent material. Figure 2 shows the contours of principal stress and strain for homogeneous and mismatched ($M = 1.5$) specimens at the same far-field J for an interface crack located along the fusion line[1]. Higher triaxial stress builds up in softer material, and over larger regions, compared with 'homogeneous' crack-tip conditions. Deformation is preferentially focussed in a lobe within the soft material. Hence it is not clear what parameters characterize the crack-tip stress and deformation fields. Further, to understand how the crack-tip stress and deformation fields drive the microstructural fracture processes (eg: cleavage, void growth, interface decohesion), it is necessary to construct models of crack-tip fields which are informative, accurately descriptive and tractable.

Here, stress fields near a longitudinal interface crack subjected to Mode-I loading under well-contained yielding are analyzed for non-hardening and low hardening materials. Local measures of stress and deformation intensity are constructed, and their effects on cleavage fracture are studied.

SLIP-LINE MODEL FOR MISMATCHED SPECIMENS NON-HARDENING CASE

For a deeply-cracked homogeneous structure with elastic/perfectly-plastic behavior, subjected to Mode-I loading, Du and Hancock [5] showed that the modified Prandtl field shown in Fig. 4a provides a good approximation for the stress-field ahead of the crack-tip. They showed that geometry-related effects characterized by the T-stress can be modelled as a change in the fan angle, δ, from that of the Prandtl field. The peak normal stress occurs ahead of the crack-tip and is given by $\frac{\sigma_{\theta\theta}}{\sigma_0}\,|_{\theta=0} = (2+\pi-2\delta)/\sqrt{3}$, while the maximum triaxiality there is given by $\frac{\sigma_{kk}}{3\sigma_0}\,|_{\theta=0} = (1+\pi-2\delta)/\sqrt{3}$. The classical Prandtl field can be recovered by setting $\delta = 0$.

A variation of the homogeneous slip-line field solution proposed for small mismatches by Ganti et al. [6] is shown in Fig. 4b. Due to strength mismatch, $M \equiv \frac{\sigma_0^H}{\sigma_0^S}$, which is defined as the ratio of yield strengths between the hard (H) and soft (S) materials, the normalized $T-$stresses are related by $T = \tau^S \sigma_0^S = \tau^H \sigma_0^H$. The stress fields are

[1]Here, the HAZ is neglected in the model. This is valid for characterizing the stress and strain fields as long as the thickness of HAZ is much smaller than the plastic zone size.

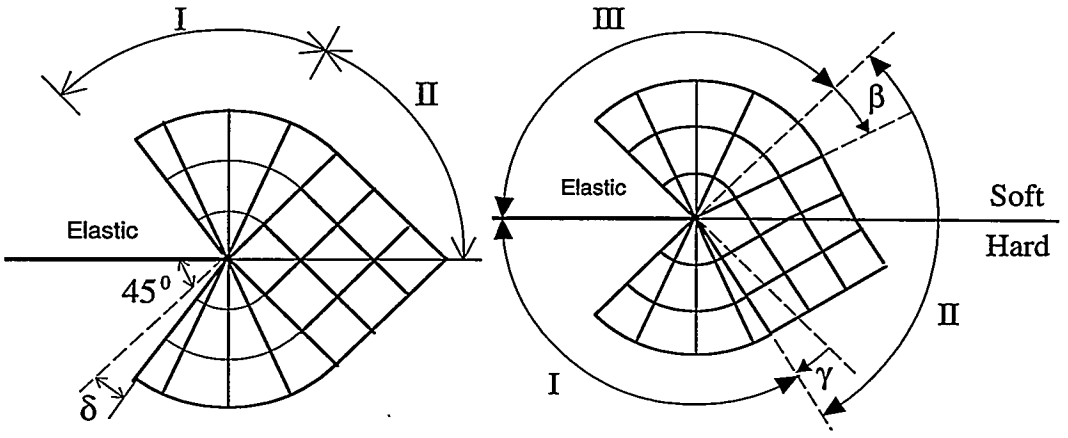

Figure 4: Modified Prandtl field for a (a) homogeneous specimen, (b) mismatched specimen.

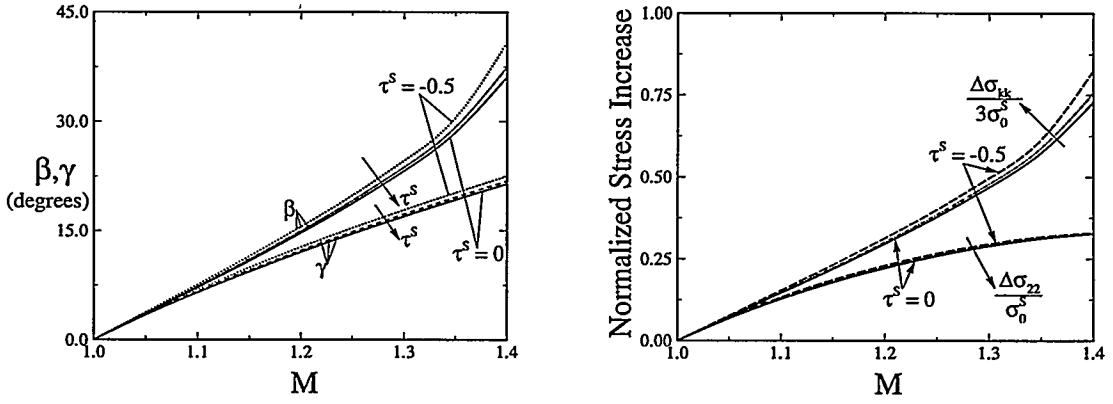

Figure 5: (a)Variation of mismatch field angles, β and γ, with mismatch, M, for various normalized T-stresses. (b)Increase in mean and normal stresses in the soft material near the interface with mismatch, M. $\Delta\sigma_{ij} = \sigma_{ij}^{mis} - \sigma_{ij}^{hom}$

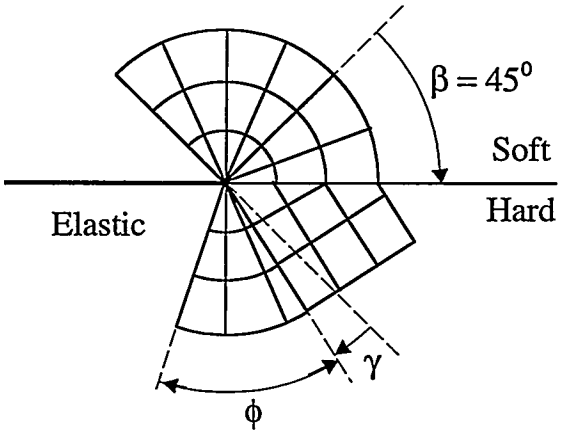

Figure 6: Modified Prandtl field for highly mismatched specimens ($M > 1.421$).

characterized by the angles β and γ which are functions of mismatch, M (Fig. 5a). The ratio of σ_{12}/σ_{22} at the interface increases with increasing mismatch and saturates at a value of $1/(1+\frac{3\pi}{2}-2\delta)$. The increases in triaxial and interface-normal stresses in the soft material near the interface are plotted in Fig. 5b. The effect of $T-$stress on the mismatch angles is of second order, as can be seen from Fig. 5a, though there is considerable reduction in the normal stress ahead of the crack tip. The fields described by Fig. 4b exist when $M \leq 1.421$. For $M > 1.421$, the fan in the soft material is completely developed, with $\beta = 45°$ and a slip-line field shown in Fig. 6 exists.

The non-hardening angular stress distributions, which can be derived from the proposed slip-line solutions, show three distinct regions for small mismatches ($M \leq 1.421$) as shown in Figures 7(a) and 7(b). In regions I and III, the stress-field is same as that of the corresponding homogeneous material, while in region II, mismatch fields differ from the homogeneous fields. Figures 7a and 7b compare the mismatch fields (14–15) with the finite element solutions. Details of the finite element solutions are given by Ganti et al [6]. The slip-line solutions are in good agreement with the corresponding finite element solutions. There is an increase in peak stress triaxiality, and more deformation is forced into the lobe of the softer material with increasing mismatch.

LOW HARDENING MATERIALS

The J-integral gives a combined measure of deformation and stress intensities in homogenoeus hardening materials. As noted in Figures 2–3, soft (hard) material experiences higher (lower) deformation than the corresponding homogeneous material, suggesting that different intensity parameters govern the local fields in each material. Equivalent J-type contour integrals, J_S and J_H, are developed which govern the stress intensity in the soft and hard materials, respectively. A schematic of the contour integrals is shown in Figure 8a. Since the interface is parallel to the crack plane, J_S and J_H are related to J by

$$2J = J_H + J_S. \tag{1}$$

In the case of homogeneous materials, $J_S = J_H = J$. Figure 8b shows the normalized radial variation of J_S with mismatch. The materials used have similar elastic properties and hardening exponent, n, but differing yield strengths. While J showed only small variation with r, the radial variation of J_H and J_S extends to tens of $CTOD$s, giving credibility to the existence of the new fields. Characterization of local deformation intensity parameters quantitatively gives the amount of shielding in the harder material and, conversely, the increased propensity for fracture in the softer material. The degree of deformation redistribution increases with increasing M.

Approximate mismatch fields for low hardening materials are developed based on an effective mismatch and defining an equivalent elastic-plastic problem for which the angular distributions are already discussed. The differing levels of deformation on either side of the interface due to the local J's (and the mismatch itself) change the effective mismatch experienced by the crack-tip. If the SSY fields characterized by J_H and J_S are scaled to satisfy approximately interface traction continuity, we can define effective mismatch as follows:

$$M_{eff} = \frac{\sigma_{\theta\theta}^{SSY(H)}\left(r/(J_H/\sigma_0^H), \theta = 0°\right)}{\sigma_{\theta\theta}^{SSY(S)}\left(r/(J_S/\sigma_0^S), \theta = 0°\right)}, \tag{2}$$

each stress being evaluated in the respective homogeneous material. For non-hardening materials, $M_{eff} = M$. Following an approach similar to that of the non-hardening

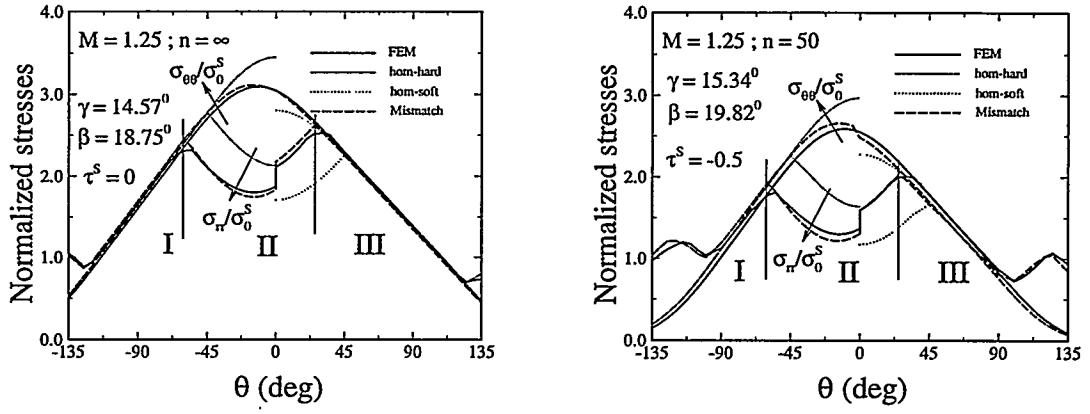

Figure 7: Circumferential variation of radial and hoop stress for (a) $\tau = 0$ and $M = 1.25$ at $r = 2J/\sigma_0^S$ (b) $\tau^S = -0.5$ and $M = 1.25$ at $r = 2J/\sigma_0^S$.

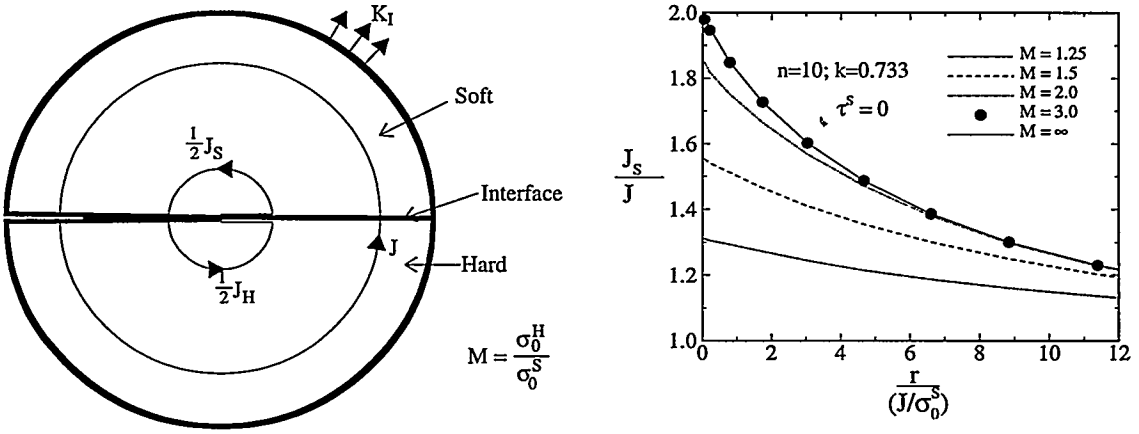

Figure 8: (a)Definition of contour integrals for mismatched specimens. (b)Normalized radial variation of J_S for $\tau = 0$.

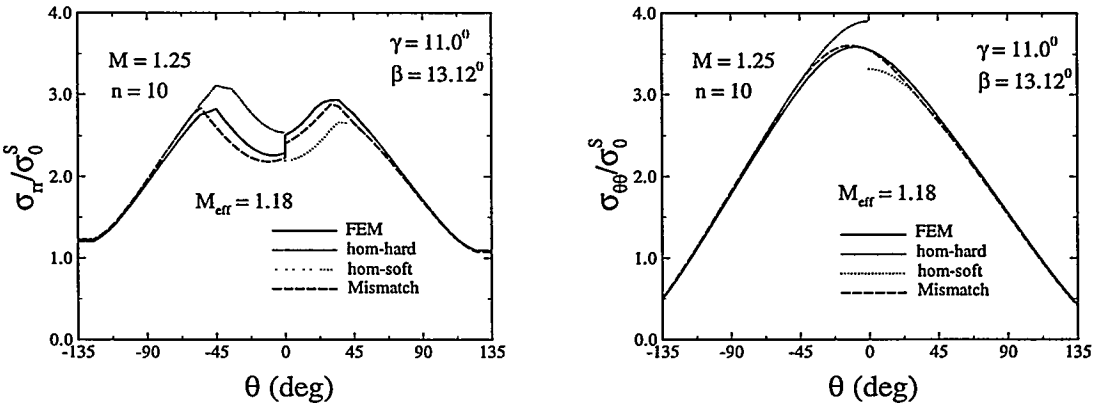

Figure 9: Circumferential variation of normalized radial and hoop stresses at $r = 2J/\sigma_0^S$ for $M = 1.25$. (a) normalized radial stress (b) normalized hoop stress.

materials, the approximate stress distributions in the soft and hard materials are developed. In region I, the solution is the homogeneous SSY one scaled by J_H, and in region III, the local homogeneous solution is scaled by J_S. In region II, the deformation intensities J_H and J_S combine to scale the fields, while the angular distribution is governed by mismatch angles, β and γ, calculated as if the materials are elastic/perfectly-plastic with an effective mismatch of M_{eff}. Figures 8–9 show the simulated and finite element results of the stress fields for different mismatches at the normalized distance $r/(J/\sigma_0^S) = 2$. The agreement between the finite element solutions and the approximate fields is excellent.

CLEAVAGE STUDIES

In the brittle to ductile transition regime for steels, the material resistance is governed by the competition between fracture by cleavage and ductile tearing. Higher stressed volumes as in mismatched specimens (Fig. 2) can bias fracture towards catastrophic failure. Here, neglecting HAZ, we study the effects of mismatch on the cleavage probability of the base metal using weakest link statistics. Assuming a three-parameter Weibull distribution for the strength distribution of the carbide particles [7], the relation between the critical J for cleavage of base metal with an overmatch, J_{Ic}^M, and that of homogeneous base metal, J_{Ic}^H, in contained yielding is given as

$$\frac{J_{Ic}^M}{J_{Ic}^H} = \frac{\left(\int^{A_H} \left(\frac{\sigma-\sigma_u}{\sigma_0}\right)^m dA\right)^{0.5}}{\left(\int^{A_M} \left(\frac{\sigma-\sigma_u}{\sigma_0}\right)^m dA\right)^{0.5}}, \tag{3}$$

where σ_u, σ_0 and m are the parameters for Weibull distribution, A_H is the cross-sectional area of the plastic zone in the homogeneous material, and A_M is the area on the soft side of the mismatched specimen. Equation 3 shows that the critical J is a function of the high-stressed volume, the stress distribution and the material parameters. Figure 11 shows the contours of the stressed areas for the homogeneous and mismatched materials. Note that for homogeneous case, only one-half the area is shown. Figure 12 shows the normalized J_{Ic}^M for mismatched materials for different threshold and Weibull exponents. The cleavage stress decreases with mismatch for large threshold stresses, while there is a moderate increase in J_{Ic} for small threshold stress and mismatch.

CONCLUSIONS

The applicability of homogeneous fracture mechanics to strength-mismatched interface cracks is addressed. New crack-tip stress fields and relevant deformation intensity measures are developed for interface cracks in strength-mismatched specimens. The stress and deformation intensities locally experienced by materials are different from those experienced in homogeneous specimens of either material, when mismatched and homogeneous specimens are loaded to a given applied J. The crack-tip fields in the soft material near the interface show higher normal and mean stresses than the corresponding homogeneous material. Our analysis shows that triaxial constraint increases almost linearly with mismatch, reaching a saturation at $M = 1.421$ in the non-hardening materials.

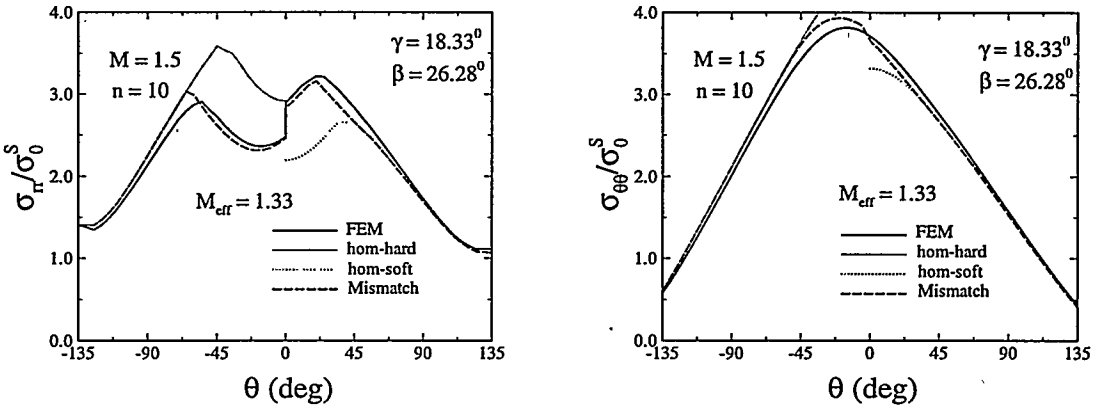

Figure 10: Circumferential variation of normalized radial and hoop stresses at $r = 2J/\sigma_0^S$ for $M = 1.5$. (a) normalized radial stress (b) normalized hoop stress.

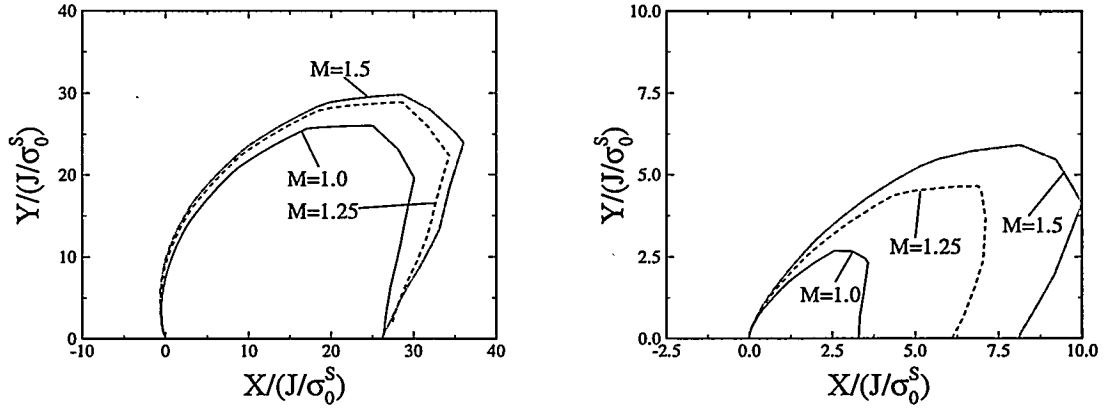

Figure 11: Contours of maximum principal stress for $M = 1, 1.25, 1.5$. (a) $\sigma_I/\sigma_0^S = 2.0$ (b) $\sigma_I/\sigma_0^S = 3.0$.

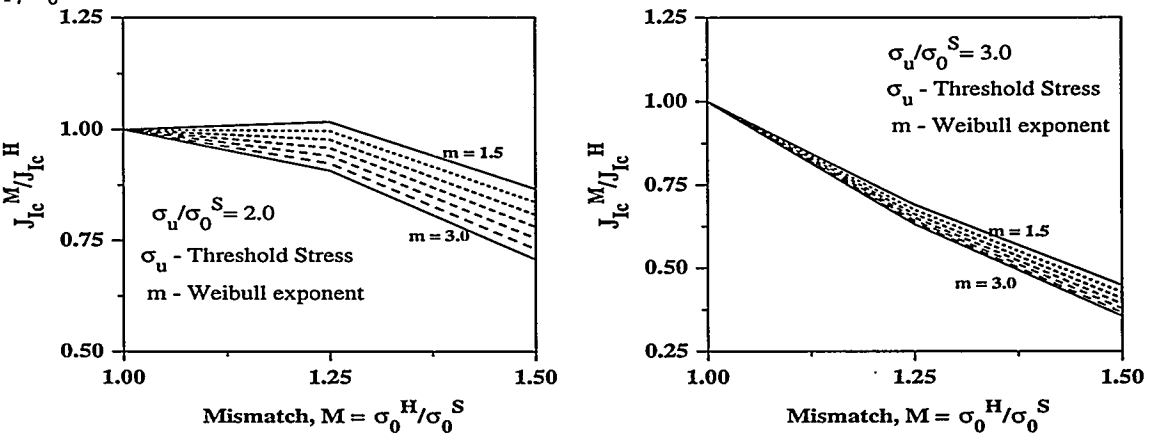

Figure 12: Normalized variation of cleavage J for different threshold stresses. (a) $\sigma_u/\sigma_0 = 2.0$ (b) $\sigma_u/\sigma_0 = 3.0$.

Cleavage studies conducted on the interface cracks in contained yielding show considerable effect of the toughness of the joint on the mismatch, M. In particular, it decreases with increasing M, eventhough, the total area of the plastic zone in the soft material is lower than that in the homogeneous material. This effect is prominent for larger threshold stresses and higher mismatches. Further results in characterization of crack-tip mismatch fields, and in modeling their effects on fracture, are also underway and will be reported elasewhere.

ACKNOWLEDGMENTS

This work was supported by the Office of Basic Energy Sciences, Department of Energy, under Grant $\#DE-FG02-85ER13331$. Computations were performed on Hewlett Packard workstations obtained under the DOE grant and under NSF Grant $\#DDM-8914161$. The ABAQUS finite element program was made available under academic license from Hibbitt, Karlsson, and Sorensen, Inc., Pawtucket, RI. We would like to thank Dr. Simona Socrate and Ms. Hong Dai for the use of their computer programs.

REFERENCES

[1] KOÇAK, M., CHEN, L., TERLINDE, G., GNIRSS, G. and SCHWALBE, K. H., "CTOD testing of HAZ and analysis of pop-in behavior," *Proc. of the 7th Int. Conf. on Offshore Mechanics and Arctic Engineering*, ASME, 1988, pp. 297–304.

[2] TOYODA, M. and SATOH, K., "Fracture toughness of welds: The incidence of mechanical heterogeneity in the correlation of toughness parameters," *Welding in the world*, Vol. 22, No. 3/4, 1984, pp. 76–86.

[3] TOYODA, M., MINAMI, F., RUGGIERI, C., THAULOW, C. and HAUGE, M., "Fracture Property of HAZ-Notched weld joint with mechanical mis-matching-Part I," in *Mismatching of welds, ESIS 17*, Eds. Schwalbe, K. H., Koçak, M., Mechanical Engineering Publications, London, 1994, pp. 399–415.

[4] THAULOW, C., PAAUW, A. J., HAUGE, M., TOYODA, M. and MINAMI, F., "Fracture Property of HAZ-Notched weld joint with mechanical mis-matching-Part II," in *Mismatching of welds, ESIS 17*, Eds. Schwalbe, K. H., Koçak, M., Mechanical Engineering Publications, London, 1994, pp. 417–432.

[5] DU, Z. Z., and HANCOCK, J. W., "The Effect of Non-Singular Stresses on Crack-tip Constraint," *Journal of the Mechanics and Physics of Solids*, Vol. 39, 1991, pp. 555–567.

[6] GANTI, S., PARKS, D. M. and McCLINTOCK, F. A "Analysis of Strength-Mismatched Interface Cracks in SSY," to be published in *Mismatch'96*, Eds. Schwalbe, K. H., Koçak, M.

[7] WANG, Y. Y., "A two parameter characterization of elastic-plastic crack-tip fields and applications to cleavage fracture," *Ph. D.* Thesis, Department of Mechanical Engineering, Massachusetts Institute of Technology, 1991.